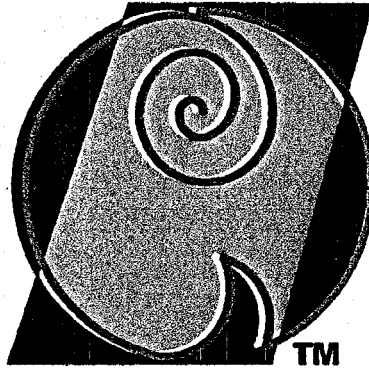DOE/ER/86100-1

Airak Inc. ™

Your Complete Monitoring Solution

FINAL REPORT

STTR PHASE 2 GRANT NO. DE-FG02-99ER86100

"THIN-FILM FIBER OPTIC SENSORS FOR POWER CONTROL AND FAULT DETECTION"

DISTRIBUTION STATEMENT: Unlimited distribution is authorized

Contact: Paul Grems Duncan
9058 Euclid Avenue
Manassas, VA 20110-5308
voice: (703) 330-4961
fax: (703) 330-4879
cellular: (703) 509-5332
pduncan@airak.com

DISCLAIMER

DISCLAIMER

Portions of this document may be illegible in electronic image products. Images are produced from the best available original document.

1. Acknowledgments

Airak, Inc. would like to thank the following organizations and personnel for the direct and significant efforts put forward in this research:

- Dr. Alec Bulawka, Program Manager, U.S. Department of Energy, Program Manager

- Dr. Jason S. Lai, Virginia Tech, Blacksburg, VA: subcontract program administration, APCS system concept;

- Mr. Leonard G. Leslie, Jr., formally with Virginia Tech, now with Northrop-Grumman Electronic Systems Power and Control Systems, Sykesville, MD, outstanding performance, APCS power electronics technical design, APCS testbed analysis, report drafting, and general engineering support;

- Mr. Stuart Samuelson, President, Deltronic Crystal Industries, Dover, NJ: Faraday crystal preparation and tailoring;

- Mr. Miron Yoplanski, President, MODIS Inc., Reston, VA: Faraday crystal tailoring;

- Dr. G.Q. Lu, Materials Science & Engineering, Virginia Tech, Blacksburg, VA: subcontract program administration, sol-gel fabrication concepts, EO-HPEM implementation, testing, and analysis;

- Mr. John Bai, Materials Science & Engineering, Virginia Tech, Blacksburg, VA: Faraday sensor characterization, EO-HPEM implementation, testing, and analysis.

- Mr. Anders DiBiccari, Materials Science & Engineering, Virginia Tech, Blacksburg, VA: sol-gel fabrication, testing, and analysis;

- Dr. Tao Lin, Mathematics Department, Virginia Tech, Blacksburg, VA: EO-HPEM electro-magnetic modeling and analysis;

- Mr. Italo Travez, President, Prototype Productions, Inc., Ashburn, VA: Fiber Optic Current Sensor Development Support;

- Mr. Ben Feldman, Vice President, Prototype Productions, Inc., Ashburn, VA: Fiber Optic Current Sensor Development Support;

- Mr. Scott Tilton, Prototype Productions, Inc., Ashburn, VA: Fiber Optic Current Sensor Development Support; and

- Mr. John A. Schroeder, Vice President, Airak, Inc., Manassas, VA: General engineering support.

2. DOE STTR Phase 2 Research Final Report Overview

The overall intent of the Phase 2 research was to:

- Develop a high-power (>10kW) active power conditioning system (APCS) testbed for photovoltaic or battery-supported applications that will correct for non-linear load currents, using fiber optic magnetic field sensing technology to provide high-bandwidth, load-current waveform information to the control circuitry, and

- Develop an electro-optical hybrid power electronics module (EO-HPEM) that contains an embedded optical magnetic field sensor element to monitor and control power delivery through the device.

2.1 PHASE 2 RESEARCH CONDUCTED & RESULTS

Table 1 summarizes the original Phase 2 research goals, and is followed by a listing of additional work that was conducted.

Table 1. Phase 2 research objectives and results.

Objectives	Results
Task 1: Determine the Active Power Conditioning System Test Bed Performance and Interface Requirements	√ Completed.
Task 2: Design, Develop, and Test the Electro-Optical Subsystem	√ Completed.
Task 3: Design, Develop, and Test the APCS Testbed	√ Completed with limitations
Task 4: Integrate and Test the Electro-Optical and Power Electronic Subsystems.	√ Attempted.
Task 5: Compare/Contrast Advantages of Fiber Optic Sensing Configuration Over Conventional Sensing and Control Loop Methodologies	√ Completed only with respect to performance to conventional sensors. Unable to complete for closed-loop operation.
Task 6: Deliver APCS Testbed to NSWC for Independent Performance Validation and PEBB Interfacing	√ NSWCCD only wanted the fiber sensors, not the APCS Testbed. Successfully completed.
Task 7: Develop Sol-Gel Thin-Film Materials and Characterize Same	√ Completed.
Task 8: Design and Model Electro-Optic Hybrid Power Electronics Module	√ Completed.
Task 9: Design and Fabricate Electro-Optic Hybrid Power Electronics Module Optical Support System	√ Completed.
Task 10: Integrate & Demonstrate Electro-Optic Power Electronics Module	√ Completed.

Additionally, the Phase 2 program accomplished the following:

1) √ development of a pre-production optical current sensor for electrical current monitoring,

2) √ partially funded 3 students at Virginia Tech during the performance of their Master's Degree requirements, and funded full-time one student, resulting in the award of his Master's Degree.

3. Task 1: Determine APCS Testbed Performance Requirements.

3.1 MOTIVATION

The motivation for this work was to design a digitally controlled, combination active filter and photovoltaic (PV) generation system. The basic system structure, shown as a block diagram in Figure 1 consisted of a 0.9 kW PV array with a nominal output voltage of 56 V, interfaced to the 360 V DC link by an isolated full bridge converter.
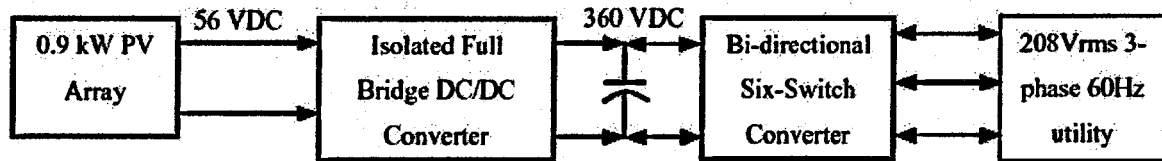
Figure 1. PV/Active Filter System Block Diagram.

The DC link was then connected to a bi-directional six-switch converter that would allow the energy generated by the PV array to be sent to the three phase utility grid at 208 V line to line. The bi-directional converter allows the system to provide active filtering capabilities, both during PV generation and when the PV energy is not available. The effective control of an active filter to correct for higher order harmonics requires that the bandwidth of the controller be as high as possible therefore the overall controller delay, which includes sensor delay, is minimized. Because of the importance of delay, this application was chosen as a suitable platform for demonstrating the suitability of the fiber optic sensors to control applications. This work involves the design and analysis of the control scheme for this system, the implementation of the active filter part of the system, and the limitations of active harmonic compensation. The PV portion of the system was not implemented due to a design problem.

3.2 ACTIVE FILTER CONTROL STRATEGIES

The active filter relies on the control system to perform the required tasks. The controls of the systems are implemented in three stages: signal conditioning, compensation, and generation of the gating signals for the switching network[1]. The first stage involves the sensing and conditioning of voltages and currents in the system so that they can be used to complete the remainder of the control functions. The second stage is the development of the required compensating signals from the information obtained in the first stage of the controller. There are two basic classifications of the methods that have been developed to accomplish this task, frequency domain techniques and time domain techniques. The final stage of the control scheme involves producing the proper gate signals to the switching network so that the compensating commands from stage two are injected into the power system. There are several methods of performing this task including linear based current or voltage control, sliding mode current control, hysteresis and fuzzy-based current control.

Generating the compensating signals can be the most complex part of the control system for an active filter. The literature has given many different methods of calculating the compensating currents or voltages for controlling active filters. Most of the calculation methods are computationally intensive and are therefore very difficult or impossible to implement as an analog controller. With the recent revolutions in DSP speed increase and cost reduction it has become practical to implement these complex calculations in real time digital control systems. The frequency domain methods are especially computationally intensive because they rely on performing Fourier analysis in real time. Because of this increased calculation burden, the literature seems to favor the time domain calculation methods for the compensation calculation stage of the controller. The time required to calculate the compensating components adds to the overall delay in the control system, decreasing the allowable bandwidth of the controller.

The current control method also has a large impact on the overall bandwidth of the controller. A comparison of some of the methods including the linear rotating reference frame current controller, digital deadbeat current controller, and hysteresis current controller as been documented[2]. The results from the comparison showed that the best results were achieved with the hysteresis controller because the delay inherent in the controller was the least. A large number of the control methods proposed for active filters utilize the hysteresis method for the current control, but this method does have some drawbacks. When hysteresis based current control is used, the switching frequency of the converter is not fixed but varies stochastically during the converter operation. This varying switching frequency can lead to difficulty when sizing the output inductors of the active filter and the generation of unwanted resonance on the utility grid.

---

[1] B Singh, K. Al-Haddad, and A Chandra, "A Review of Active Filters for Power Quality Improvement," *IEEE Transactions on Industrial Electronics*, Vol. 46, No. 5, October 1999, pp. 960-971.

[2] S. Buso, L. Malesani, P. Mattavelli, "Comparison of Current Control Techniques for Active Filter Applications," IEEE Transactions on Industrial Electronics, Vol. 45, No. 5, October 1998, Pg. 722-729.

There are a multitude of different methods that have been proposed for the control of an active filter. Some of the methods combine and or simplify the three steps listed before that are necessary for a control scheme. One example is the Unified Constant Frequency Integration Control method[3]. This method has a fast response and a constant frequency so the problems with hysteresis are avoided.

4. Task 2: Design, Develop, and Test the Electro-Optical Subsystem.

This section of the report describes the fiber optic current transducer that was designed as part of the APCS development effort.

4.1 PRIMARY FUNCTION

Airak's fiber optic electrical current transducer (FOECT) is designed to replace existing current sensors, transducers, and instrument transformers in applications ranging from monitoring load currents in electrical power lines to providing feedback information in high-energy power electronic converters. The FOECT is extensively used in applications requiring intrinsic voltage isolation, immunity from electromagnetic interference, or where physical constraints preclude the use of conventional Hall, toroidal, or other current measurement devices.

The FOECT can support measurement of currents ranging from a few milliamperes to tens of thousands of amperes with negligible change in size or weight. Each transducer uses an extremely small, lightweight optical crystal to measure the current within a given range. Varying the thickness of the crystal permits variations in the measurement range. The implications of this are enormous—a 15 kV, 1000 A transformer weighing 324 pounds can now be replaced with a transducer weighing *28 grams*. Furthermore, because the entire FOECT assembly uses standardized components, large cost reductions for the units can be realized due to economies of scale resulting from high-volume manufacturing.

4.2 SECONDARY FUNCTION

Airak's FOECT also serves an important secondary function—it measures the temperature of the surrounding environment. This function is described in detail below and has important implications (*e.g.*, a single transducer can simultaneously monitor both the magnitude of a load current passing through a conductor and the temperature of the conductor, which helps to optimize power delivery operations).

4.3 BASIC THEORY OF OPERATION

The method of using optical crystals to detect a change in a magnetic field is not new. More than 150 years ago Sir Michael Faraday discovered that when linearly polarized light traveled through flint glass that was exposed to a magnetic field its plane of polarization rotated. This property, now known as the Faraday effect, is widely used in the fiber optic telecommunications field to prevent reflected light energy from coupling back into a light source and changing source parameters such as frequency or power output. If the Faraday material is placed in the path of a magnetic field, such as one generated by current flow, the plane of polarization rotates in a known and predictable fashion. By monitoring the rotation of the incident polarization state, a direct measurement of the magnetic field intensity can be inferred. The relationship governing this phenomenon is best stated as:

$$\Theta = VHl$$

where Θ is the measured angle of rotation of the field, V is a constant known as Verdet's constant, H is the applied magnetic field, and l is the optical path length. All crystalline materials exhibit the Faraday effect, but the magnitude varies greatly. For example, the Verdet constant for a SiO_2 crystal (e.g. optical fiber) is approximately 3.2 e-4 (deg/cm-Oe), while in ferromagnets (*e.g.* such as used by Airak) the value can be on the order of 6.0 e+5 (deg/cm-Oe). Equation (1) is important because it states that the Faraday rotation Θ, and hence sensitivity of the crystal, increases as the Verdet constant increases. It also states that the longer the optical path length l, the more Faraday rotation (sensitivity) that will result for a given field. Both of these parameters are important in designing the transducer because they give Airak two degrees of freedom to optimize a sensor for a particular application.

---

[3] C. Qiao, T. Jin, and K. M. Smedley, "Unified Constant-frequency Integration of Three-phase Active-power Filter with Vector Operation," Power Electronics Specialists Conference, Vol. 3, 2001 Pg. 1608-1614.

Existing optical current sensors now on the market use a method of measuring current that is radically different from the technology that Airak has developed. These sensors use either bulk optical crystals or long lengths of optical fiber to encircle the current-carrying conductor. When an optical path completely encircles a conductor, a numerical integration can be performed about the optical path that directly relates the Faraday rotation to the current flowing through the optical path. In this instance, the rotation is related to current I by a form of Ampere's Law:

$$\Theta = V \oint H dl$$

$$\Theta = VI$$

Finally, if N optical paths exist around the conductor, the total current in the conductor is

$$I = \frac{\Theta}{VN}$$

Applications that require higher sensitivity wrap a higher number of optical fiber turns around the conductor being monitored. Two companies, NxtPhase (www.nxtphase.com) and KVH (www.kvh.com) are exploiting this approach for electrical power markets (see Section 10).

Using optical fiber as a sensor method is impractical in many applications because it is not feasible to interrupt power by disconnecting the conductor, installing the fiber coil assembly, and then reconnecting the conductor. Another disadvantage of an all-fiber sensor is that in practical use, the 1000+ loops that comprise the fiber coil assembly that encircle the conductor can be no smaller than 4-5 cm in diameter – which significantly limits application of the technology to larger wires. Violation of this condition typically results in extremely high temperature sensitivity, which then appears as an undesired rotation of the state of polarization of the desired signal.

Bulk glass is another material that exhibits a Faraday effect. An advantage of the use of bulk glass is that the sensor can be fabricated from materials with a higher Verdet constant than normal optical fiber, which improves the sensitivity to the influencing magnetic field. These bulk crystals can be annealed by heating them slowly in an oven, letting them bake, then slowly cooling, which can release internal stresses. Reducing internal stresses improves the optical and mechanical properties of the crystal, which is desirable for manufacturing as well as calibration. By themselves bulk-glass sensors are relatively mechanically stable both in temperature and mechanical handling. Bulk glass can be made relatively inexpensive, which portends well for mass production concepts using these sensors. ABB (www.abb.com) is one company that has produced products using this approach (see Section 10).

Despite these apparent advantages over optical fiber, bulk-glass sensors suffer from their own set of limitations. The transducers manufactured from bulk glass are large, relatively on the same order as the all-optical fiber sensors previously described. Bulk glasses are not ferromagnetic, hence their Verdet constants are lower than the latest crystalline materials, which restricts their applications to extremely high current measurement. Additionally, obtaining multiple circular paths around a bulk-glass arrangement in order to increase the sensitivity of the sensor has been accomplished by some researchers, but there are limitations of using this configuration in applications that experience tremendous temperature fluctuations. Finally, assembly and alignment of bulk-glass sensors has historically been performed by hand, resulting in tremendous labor costs that preclude their widespread use.

As previously stated, ferromagnetic materials (e.g., bismuth- and terbium-doped yttrium-iron-garnet $(BiTb_2Y_3Fe_5O_{12})$) have much larger Verdet constants per unit thickness than simple fiber optic cable or bulk-optic crystals. The result of using ferromagnetic materials is that a much smaller Faraday rotator is required to measure a given magnetic field strength, and the outcome is that a whole class of reduced-size magneto-optical transducers is enabled. Methods to grow these materials are well established and directly support other markets, specifically optical telecommunications, hence tremendous economies of scale are realized that surpass that of bulk-glass and rival the cost of optical fiber.

Airak's optical technology (shown in Figure 1) differs significantly from both the optical fiber and bulk-glass technologies described above. Specifically, it is not necessary for the transducer to completely encircle the conductor being monitored. Rather than perform an integration of the magnetic field, the sensor samples a point in the magnetic field using a crystal at a location that is predetermined by the sensor holder (see Appendix A for a more detailed drawings and further explanation). Furthermore, because the magnetic field is generally uniform in magnitude near the surface of a circular conductor, the sensor's physical location on the conductor is irrelevant.

The use of highly sensitive Faraday materials and Airak's configuration also enables interesting capabilities not available with either optical fiber or bulk-glass methods of current sensing.

Figure 2. *Airak's optical current transducer and cable support clamps attached to a 4/0 AWG conductor.*

$$V(\lambda_0) = -B \frac{\pi \gamma}{\lambda_o n_o}$$

Equation (5) shows an interesting relationship between the Verdet constant and the wavelength of the light passing through the Faraday crystal (ignore the other variables for the purposes of this discussion). It basically states that the Verdet constant is a function of the wavelength (color) of the light; hence TWO different values of the Verdet constant will be reported if the wavelength is changed and everything else remains constant. **This very important relationship can be exploited to simultaneously measure current and temperature.** Due to the Verdet constant's dependence on wavelength, we now have two equations and two unknowns,

$$\Theta(\lambda_1) = C_1 \cdot dB + C_2 \cdot dT$$

$$\Theta(\lambda_2) = C_3 \cdot dB + C_4 \cdot dT$$

where $\Theta(\lambda_1)$ is the total rotation measured at one particular wavelength λ_1, $\Theta(\lambda_2)$ is the total rotation measured at another particular wavelength λ_2, dB is the desired change in magnetic flux component that contributed to the rotation $\Theta(\lambda_1)$ and $\Theta(\lambda_2)$, dT is the desired change in temperature component that contributed to the rotation $\Theta(\lambda 1)$ and $\Theta(\lambda 2)$, and C_1 through C_4 are calibration coefficients.

C_1 through C_4 are characterized during calibration and are locked into the signal processing system. For real-time operation, $\Theta(\lambda_1, \lambda_2)$ is measured, and knowing these values, the desired quantities dB and dT can be determined from:

$$dB = \frac{C_4 \Theta(\lambda_1) - C_2 \Theta(\lambda_2)}{C_1 C_4 - C_2 C_3}$$

$$dT = \frac{C_1 \Theta(\lambda_2) - C_3 \Theta(\lambda_1)}{C_1 C_4 - C_2 C_3}$$

Due to the required division a digital signal processing system is the best candidate for the electro-optic function for this type of sensor.

Having established the ability to simultaneously monitor changes in temperature, as well as changes in magnetic field, it is now possible to directly monitor the temperature of conductor as well as the load current passing through the conductor. Figure 3 shows an exploded view of Airak's integrated optical current and temperature sensor. For simplicity, only those components directly involved in the heat-transfer process are identified. As

previously established, the transducer reports the temperature of the Faraday crystal 3. The Faraday crystal is held in place by an aluminum crystal carrier 2, which is secured to an aluminum sensor body 1. If the surface of the conductor being monitored is in physical contact with the aluminum sensor body 1, then this heat is "sunk" and surrounds the Faraday crystal 3.
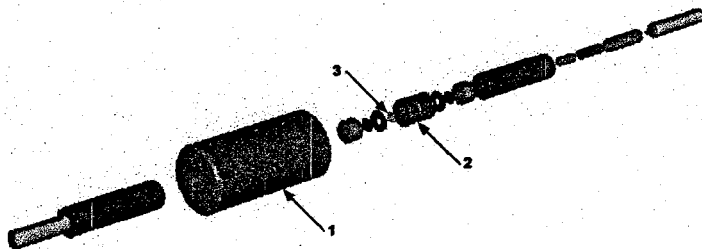

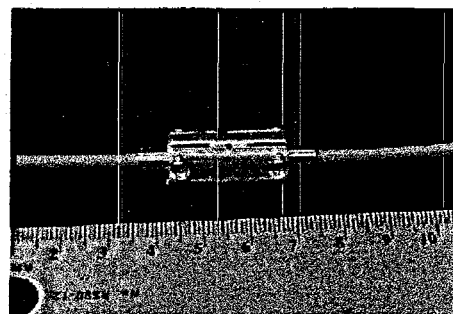Figure 3. Exploded view of Airak's integrated optical current and temperature sensor.

Figure 4. Physical dimensions of Airak's integrated optical current and temperature sensor. The major units shown are centimeters.

Figure 4 shows the physical dimensions of Airal's transducer. As shown, the aluminum sensor body is 25.4 mm long and the diameter is 12.7 mm. Support ferrules extend another 5 mm from each end of the aluminum sensor body. The device can be made smaller and lighter, which would further increase the number of possible mounting locations, but, to date, Airak has not made these modifications.

The following features distinguish the FOECT from other types of current transducers and transformers:

- **Sensor size is independent of current range.** In general, current transformers, transducers, and related sensors must be sized according to the magnitude of the current that they monitor, as well as to the magnitude of the system voltages in which they are installed. Airak's transducer, due to the inherent isolation afforded by optical fiber, does not require any special packaging or insulating below 19.2kV. Furthermore, because sensitivity is controlled by the thickness of the Faraday crystal, the overall size and weight of the transducer do not change as a function of the measurement range.

- **Frequency response is limited only by the signal processing electronics.** Traditional transducers are incapable of providing both high measurement range and high frequency response. This is a significant limitation that limits their usefulness in high voltage or high current applications, such as Transmission and Distribution (T&D) monitoring or fault location applications. Wire-wound transformers and other related devices rated for 1000 A are typically limited to less than 25 kHz response. Hall-effect devices for the same range are limited to about 250 kHz. Contrasting this, Airak's FOECT frequency response is fundamentally limited by the signal processing electronics, not the transducer[4], which suggests that it is an ideal magnetic field and current sensor for T&D monitoring, fault-current location systems, power electronics applications, and other high-power, closed-loop control and monitoring systems.

- **Transducer packaging supports automated manufacturing.** The cylindrical, symmetric design of the transducer supports automated assembly and calibration, a tremendous advance in state-of-the-art for optical fiber sensors. Automated manufacturing reduces labor and material costs, enables repeatability in calibration, and improves overall sensor reliability.

The use of optically-transparent ferromagnetic crystalline materials enables a whole new set of features for monitoring current that are not possible with conventional or commercially available optical transducers, and the result is a breakthrough technology for magnetic field or current sensing.

___

[4] Deeter, M.N., Rose, A.H., Day, G.W., "Fast, sensitive magnetic-field sensors based on the faraday-effect in YIG", J. Lightwave Tech., 8 (12), pp. 1838-1842, December 1990.
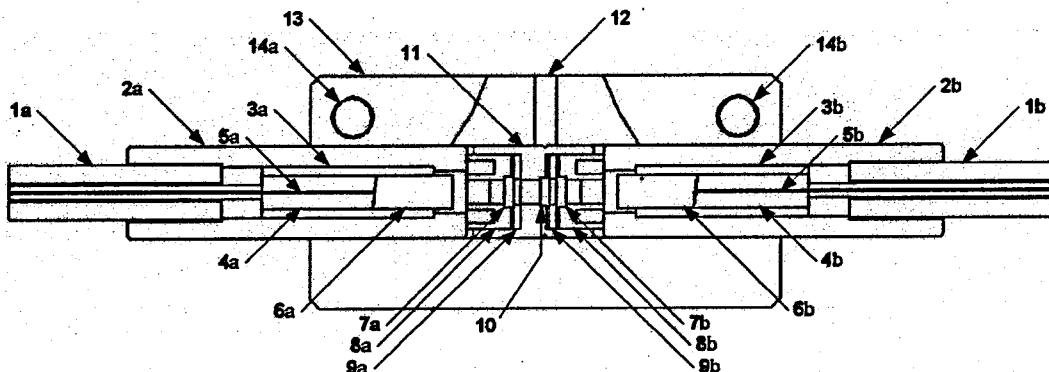
Figure 5. FOECT line art detail.

4.4 FOECT LINE ART AND DETAILS OF OPERATION

1a, 1b: Input and output furcation tube

2a, 2b: Collimator outer housing

3a, 3b: Hollow-core tube

4a, 4b: Capillary tube

5a, 5b: Input and output optical fiber

6a, 6b: GRIN lens

7a, 7b: Polarizing material

8a, 8b: Retainer/adjuster

9a, 9b: Spacer

10: Faraday rotator material

11: Faraday rotator material carrier

12: Locking pin

13: Sensor housing

14a, 14b: Sensor housing tensioning screws

4.4.1 FOECT Operation

With reference to Figure 5 and Figure 6, the device in accordance with a preferred embodiment, the invention is a transmissive magneto-optical sensor that can be operated in either non-reciprocal mode or in reciprocal mode. In non-reciprocal mode, light only travels in one direction through the current sensor assembly, whereas in reciprocal mode light travels simultaneously in opposing directions through the sensor assembly. Non-reciprocal mode can be used to simplify signal processing and to reduce system cost, whereas reciprocal mode is used where higher measurement resolution or vibration immunity is the governing goals. In either mode, optical operation of the device is the same.

The operation of the device in non-reciprocal mode is as follows. Light energy, such as that from a semiconductor laser and which represents and optical wavefront, enters the current sensor assembly through furcation tube 1a containing an internal optical fiber 5a. The optical fiber 5a is held in place via capillary tubing 4a, and the capillary tubing 4a/optical fiber 5a is optically bonded to a quarter-pitch graded index lens 6a, which expands and collimates the light beam. The capillary tubing 5a and graded index (GRIN) lens 6a are held secure in the assembly by a hollow-core tube 3a and non-ferrous collimator outer housing 2a. The light is then projected through polarizer 7a, which is held securely in place by retainer/adjuster 8a. This polarizer 7a establishes an arbitrary but fixed state of polarization for the incident optical wavefront.

The Faraday rotator material 10 is held in a preferred orientation within the sensor assembly by the Faraday rotator material carrier 11 and locking pin 12. The Faraday rotator material carrier 11 is hollow and is aligned with the propagating light wavefront from polarizer 7a. Situated between, and axially aligned with retainer/adjuster 8a and Faraday rotator material carrier 11 is a spacer 9a, which is used to slightly offset the polarizer 7a from the Faraday rotator material 10. The propagating light wavefront from polarizer 7a travels through spacer 9a, is incident upon the Faraday rotator material 10, and exits through the Faraday rotator material carrier 11. In the presence of a

magnetic field this lightwave will undergo a rotation of the polarization state established by polarizer **7a**. This rotation is proportional to the strength of the magnetic field intersecting the Faraday rotator material **10** in the same direction as the direction of the propagating lightwave.

The propagating light now passes through another spacer **9b**, which is positioned axially between the Faraday rotator material carrier **11** and another retainer/adjuster **8b**. This retainer/adjuster **8b** holds another polarizer **7b** whose transmission axis is in the same plane as polarizer **7a** but is rotationally offset by an amount that is established by the system configuration. This polarizer **7b** serves to separate the polarization rotation induced by the Faraday rotator material **10** into a polarization component that varies the intensity of the propagating wavefront as a function of the applied magnetic field. The remaining components of the sensor are a mirror image of the assembly previously described. The collimated optical wavefront from polarizer **7b** is incident upon the graded-index lens **6b** and is refocused upon the optical fiber **5b**. From here the light is sent down the optical fiber **5b** and furcation tube **1b** where is eventually converted to an electric current by a photodiode and then is processed by an electronics signal processing circuit.
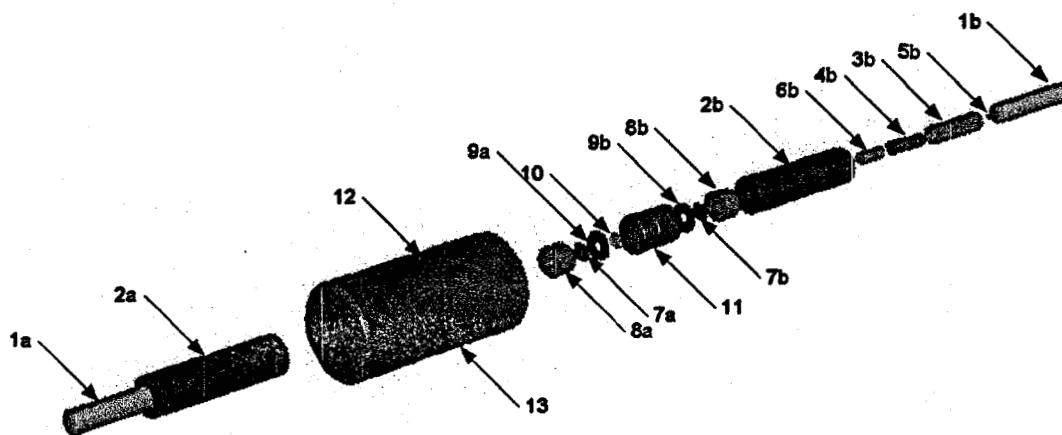
Figure 6. FOECT exploded view detail.

1a, 1b: Input and output furcation tube

2a, 2b: Collimator outer housing

3a, 3b: Hollow-core tube

4a, 4b: Capillary tube

5a, 5b: Input and output optical fiber

6a, 6b: GRIN lens

7a, 7b: Polarizing material

8a, 8b: Retainer/adjuster

9a, 9b: Spacer

10: Faraday rotator material

11: Faraday rotator material carrier

12: Locking pin

13: Sensor housing

14a, 14b: Sensor housing tensioning screws

4.5   REPRESENTATIVE FOECT ELECTRICAL CURRENT PERFORMANCE DATA
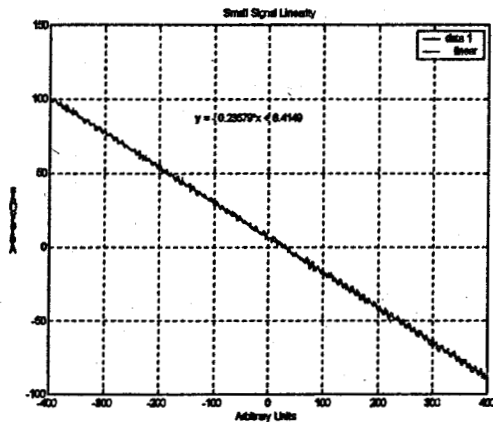
Figure 7. FOECT small-signal linearity.

Figure 7 shows the small-signal linearity of the transducer with a 60-Hz sinusoidal excitation. As can be seen, the response of the transducer is extremely linear for small variations in signal response, with a 0.99943 coefficient of correlation between the transducer output and a linear curve fit.
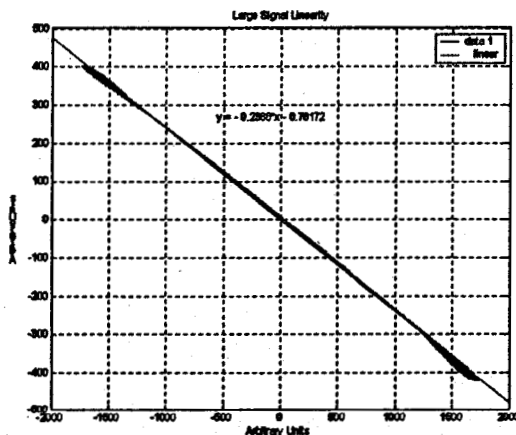
Figure 8. FOECT large-signal linearity.

Figure 8 shows the large-signal linearity of the transducer with a 60-Hz sinusoidal excitation. As can be seen the response of the transducer is linear, but as the magnitude of the excitation increases, a slight hysteresis develops. This is purely a function of the materials that comprise the Faraday rotator material and in no way limit the usefulness of the transducer. The coefficient of correlation between the transducer output and a linear curve fit is 0.9936 for the representative data shown.

5. Task 3: Design, Develop, and Test the APCS Testbed[5].

5.1 SYSTEM OVERVIEW

This section describes the hardware used to implement the APCS system. The connection of the system to the utility grid is shown in Figure 9.
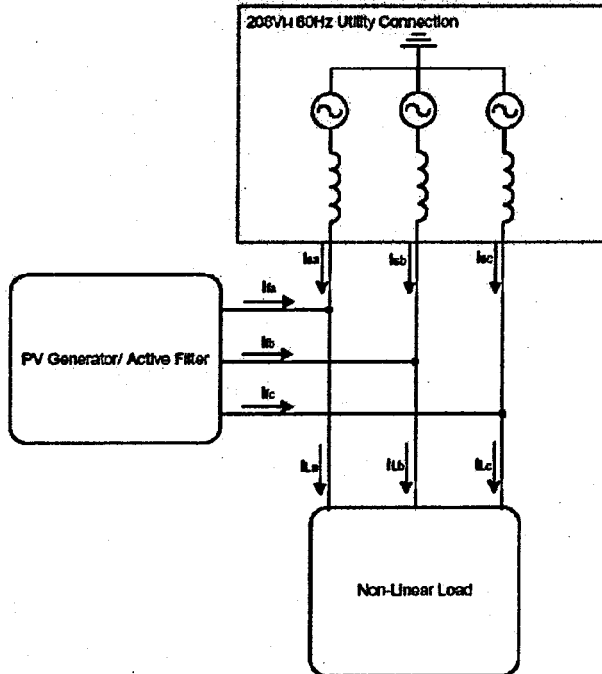
Figure 9. Block diagram of system connection to the utility and load.

---

[5] This portion of the report is taken from Chapter 2 of a thesis that resulted from this work: L. Leslie, "Design and Analysis of a Grid Connected Photovoltaic Generation System with Active Filtering Function", Master's Thesis, Virginia Polytechnic Institute & State University, March 14, 2003.

Figure 10 shows a more detailed diagram of the PV generator/ active filter section from Figure 9
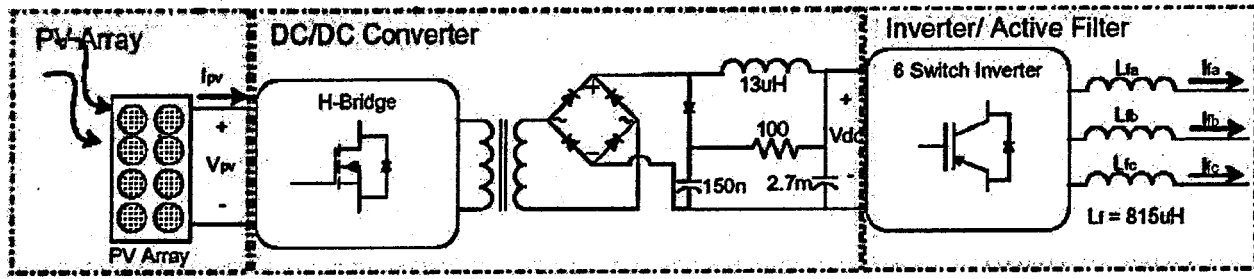
Figure 10. Block diagram of PV generator/ active filter.

Table 2 System current variables.

Variable	Description
I_{sa}, I_{sb}, I_{sc}	The currents flowing from the source (or utility).
I_{fa}, I_{fb}, I_{fc}	The currents flowing out of the PV/active filter sytem.
I_{La}, I_{Lb}, I_{Lc}	The currents flowing into the load.
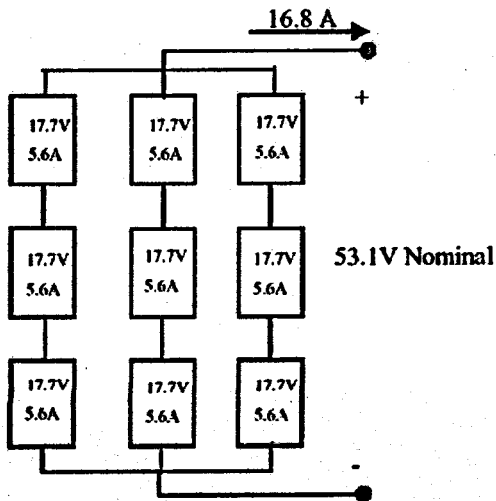
Figure 11. PV array connections.

5.2   PV ARRAY

The 0.9 kW PV array that was selected for the system consisted of three parallel connections of three Siemens SR100 panels connected in series as shown in Figure 11.

Each of the SR100 solar panels has a maximum power rating of 100W, which occurs at a rated voltage of 17.7V and a rated current of 5.6A. The panels have an open circuit voltage of 22V and a short circuit current of 6.3A. A picture of one of the panels and the V-I curve for each panel is shown in Figure 12. The V-I curves have a non-linear shape. It can be seen in the figure below that the curve tends to slide down as the solar intensity decreases, and the curve slides to the left as cell surface temperature increases. In the system design, the PV array voltage and output current are sensed by LEM voltage and hall current sensors, respectively. The voltage and current variables from the sensors are fed into the digital controller through A/D channels to be used for the MPPT control scheme.
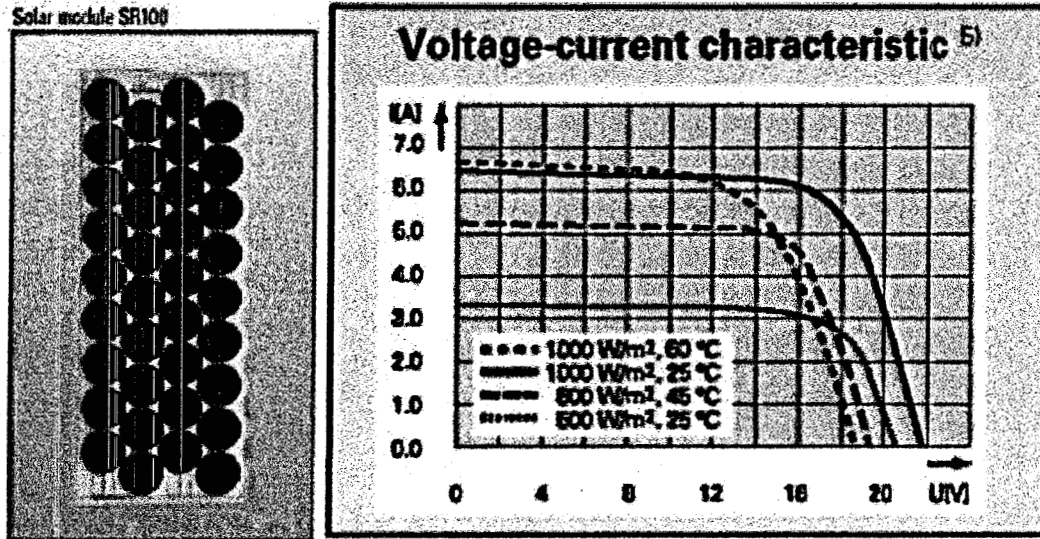
Figure 12. *Siemens 100W PV panel and V-I curves.*

5.3 DC-TO-DC CONVERTER.

The DC-to-DC converter power stage selected for the system has a topology that is an isolated full bridge implemented with 100V, 75A MOSFETs (Advanced Power Technologies APT10M19BVR). shows the schematic of the converter. The original design was for two 5kW converters operated in parallel to provide 10kW for the inverter stage. In this application the converter only needs to provide 0.9kW, so only one side of the converter is used. The board designed is shown in Figure 14 with only one side populated. The capacitor across the input of the converter shown in the schematic is actually three capacitors in the circuit as can be seen in Figure 14. The bulk capacitor helps to maintain the DC bus during transients and the commutation capacitors are placed as close to the half bridges as possible to minimize inductance, so they can prevent the output capacitance of the switches from ringing with the bus inductance during switch commutation.
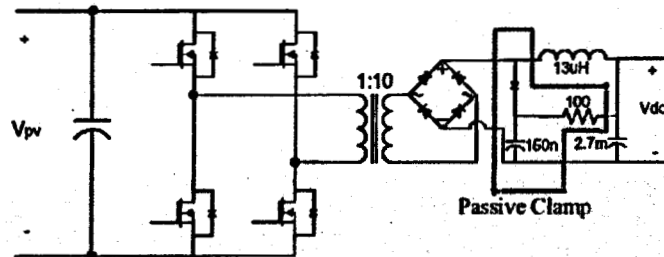
Figure 13. *DC/DC converter schematic.*

Figure 14. *DC/DC converter power stage.*

A TI UC3895 phase shift modulation control chip performs the full bridge switch modulation. The phase shift modulation scheme can provide zero voltage switching by utilizing the energy in the transformer leakage inductance

and the output filter inductor[6]. The actual control of the duty cycle of the converter is through a PWM channel from the controller that is passed through a low pass filter to act as a D/A channel and connected to the controller chip.

5.3.1 Gate Drive

The gate drivers used for the MOSFETs in this converter are the same ones used in the inverter stage so they will only be described here. Figure 2.7 shows a schematic of the gate drive.

Figure 15. Gate drive schematic.

An Agilent HCPL316J optically isolated gate drive chip was used to design the gate drive. The optical isolation of the gate drive IC provides isolation for the devices that are tied to the upper rail and allows all of the devices to be turned off with a negative voltage. In this design the gates of the devices are turned on with +15V and turned off with –5V, which are provided by the flyback power supply shown in Figure 16. The power for the gate drive power supply as well as the control circuitry is derived from the input voltage using the auxiliary power supply shown in Figure 17. The auxiliary power supply is a flyback that was designed using a Power Integrations Top Switch integrated control and MOSFET IC. The auxiliary power supply also supplies the +5V that is required to run the logic in the gate drive IC. Protection against overcurrent conditions in each device is provided by the gate drive IC with desaturation protection. The gate drive IC has a constant current source that forces a voltage drop across a resistor and diode that are connected to the collector or drain of the switching device. When the device turns on, the current source charges the blanking capacitor to the voltage across the device plus the voltage drop of the diode and the voltage drop across the resistor. The blanking capacitor charging time gives the device enough time to turn on completely. If the total voltage at the desat pin is above 7V the device is turned off and the gate drive IC feeds back a fault signal to the controller. The gate drive IC will also go into a fault condition if the gate drive power supply voltage drops below 11V. When a fault occurs, the gate drive IC must be reset run again.

Figure 16. Gate drive power supply.

---

[6] V. Vlatković, J. A. Sabaté, R. B. Ridley, F. C. Lee, and B. H. Cho, "Small-Signal Analysis of the Phase-Shifted PWM Converter," IEEE Transactions on Power Electronics, Vol. 7, No. 1, January 1992, pp.128-135.

Figure 17. Auxilliary power supply.

5.3.2   DC/DC Converter Transformer.

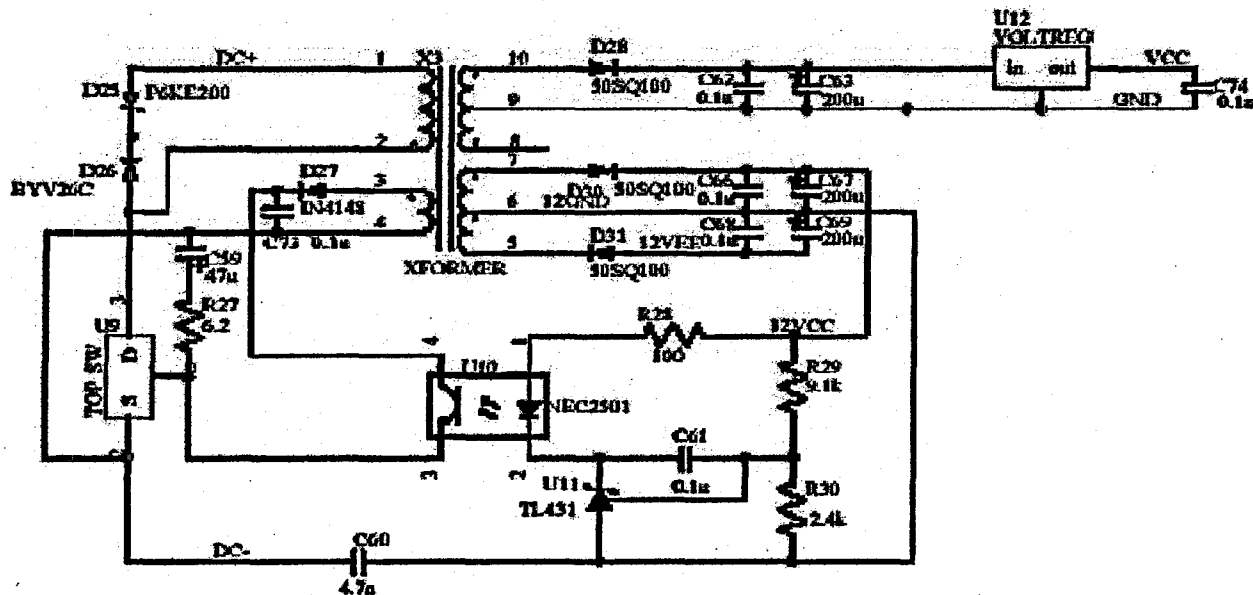The output of the DC/DC converter must be above 350V so the transformer design boosts the voltage up to this level. The transformer was designed to use an ETD-49 core and has 4 primary windings and 40 secondary windings, giving a turns ratio of 1:10.

5.3.3   Output Filter

The output filter design was based on providing enough capacitance to act as energy storage for the active filter function of the system. The calculation for the size of the DC link capacitor for the active filter is based on controlling the voltage change of the DC link under worse case operating conditions. It is assumed that when the active filter is providing compensation at the fundamental line frequency for displacement power factor (DPF) correction, then the capacitor is charged and discharged twice per line cycle and that the charge and discharge times are even. Based on a charge/discharge balance, the following equation is used to determine the capacitance value for the DC link[7]:

$$C_d = \frac{I_{f-rms}\Delta t}{\Delta V_d} = \frac{I_{f-rms}}{4 f \Delta V_d} = \frac{25}{4(60)(40)} = 2.6mF$$

The change in DC link voltage is high at 40V, but it is assumed that the control loop for the DC link voltage will help to hold a tighter voltage band. A 2.7mF, 450V aluminum electrolytic capacitor was chosen for the DC link of the system.

Based on the proposed controller, it was desired to have a wide bandwidth for the DC/DC converter output voltage loop. To help ensure a wide bandwidth was possible for the converter, the resonant point of the output filter was chosen to be 850Hz. This resonant point for the filter resulted in an inductance value of 13uH. The drawback of using this output filter design is that the DC/DC converter will always operate in the discontinuous conduction mode (DCM). By operating in DCM the major benefit of the phase shifted full bridge topology, zero voltage switching, is lost. This trade off was made to allow for the proper operation of the proposed control scheme.

---

[7] Lai, J. S., "Active Power Filtering for Harmonic Compensations," ITRI Short Course, Unit 7 on Power Quality and Three-Phase Power Factor Correction, March 16-17, 2000.

5.3.4 Passive Clamp

The outlined part in Figure 13 is a passive clamp that controls the voltage overshoot that occurs due to a resonance between the capacitance of the rectifier diodes and the leakage inductance of the transformer. The overshoot occurs when the diodes turn off, and requires that the diode voltage rating be increased. When the rectifier diodes turn off the voltage begins to rise and is clamped by the diode to prevent excessive voltages. The size of the clamp capacitor determines how high the voltage will go. After the voltage begins to decrease the clamp capacitor discharges to the nominal DC link voltage through the clamp resistor. About 60% of the clamp energy is dissipated in the resistor and the rest is delivered to the load[8].

5.4 INVERTER/ ACTIVE FILTER.

The power stage for the inverter/active filter part of the system is a 6-switch topology that is rated at 10kVA. As discussed in section 5.3.1, the same gate drive circuit is used in this power stage as the DC/DC converter. The auxiliary power supply is also the same as in the DC/DC converter. International Rectifier IRG4PSC71UD 600V, 60A IGBTs with integrated anti-parallel diodes are used as the power devices in the inverter/active filter power stage. Figure 18 shows a schematic representation of the power stage.
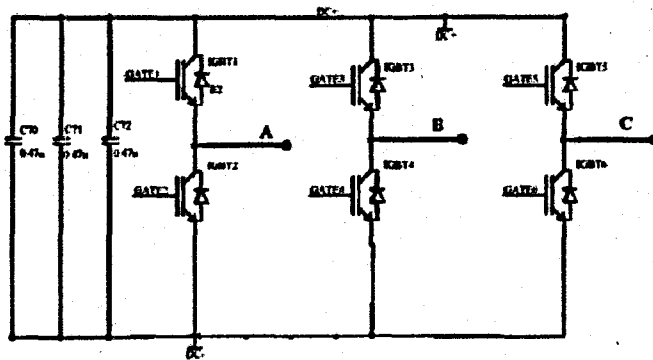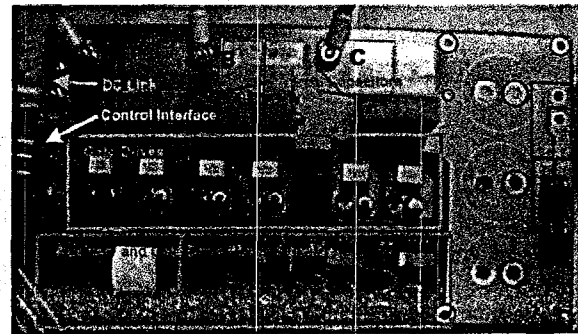

Figure 18. Inverter power stage schematic.

Figure 19. Inverter/active filter power stage.

A picture of the upper side of the power stage is shown in Figure 19. The PC board has components on both sides and the DC link bus and output buses are integrated into the PC board. The three capacitors shown across the DC link in the schematic are the commutation capacitors that are placed as close to the complementary pairs of power devices as possible to minimize voltage overshoot and ringing on device turn off.

5.4.1 Output Filter Inductors

Included as part of the inverter/active filter power stage are filter inductors that are placed in series with the three phase outputs of the power stage. The purpose of the inductors is to filter the switching components out of the output currents of the inverter/active filter. The inductor size was designed to limit the current ripple to 2.5A at a switching frequency of 32kHz, a DC link of 360V and a line-to-line output voltage of 294Vpk.

$$L_f = \frac{Vdc - Vab_{pk}}{f_s \cdot \Delta i} \approx \frac{360 - 294}{32k \cdot 2.5} = 825uH$$

To size the inductors, first a calculation was done based on the real power that could be flowing from the PV array to the grid, then an assumption was made that the 5th harmonic would be the worst case current for the active filter. Based on a 10kW non-linear load it was assumed that 5kVA of reactive power could be circulated through the active filter. It was then assumed that 60% of the 5kVA would be at the 5th harmonic and the inductors were designed

[8] L. H. Mweene, C. A. Wright, M. F. Schlecht, "A 1 kW 500 kHz Front-end Converter for a Distributed Power Supply System," IEEE Transactions on Power Electronics, Vol. 6, No. 3, July 1999, pp. 398-407.

based on that current. Two Magnetics ® MPP 58866-A2 125μ cores are used in each inductor and the windings consist of 54 turns of 3 strands of 17 gauge wire. The measured inductance of the completed inductors is 815uH. Figure 20 shows the power stage connected to the output filter inductors.

5.5 CONTROLLER HARDWARE

The controller for the system is based on a high performance Texas Instruments 32 bit floating point DSP. The particular DSP family chosen for the project was designed for communications applications, and therefore the peripherals included with the DSP do not meet the requirements for a typical power electronics control system. A third party, configurable daughter card was chosen to interface the DSP to the system.

Figure 20. Power stage with output filter inductors.

5.5.1 DSP Board.

Texas Instrument's TMS320C6701 DSP core was chosen for the controller for this system to ensure that a sufficient amount of processing power was available to not only control the system, but to also provide signal processing for the fiber optic current sensors outputs. The specifications of the DSP core are given below:

DSP core: TMS320C6701

• 32 Bit floating point processor

• 133 MHz maximum clock speed

• 32, 32 bit registers

• 8 independent function units (6 ALU's and 2 MAC's)

• Up to 8 simultaneous 32 bit fixed point instructions per cycle

• Up to 6 simultaneous 32 bit floating point operations per cycle

• Glue-less interface to synchronous and asynchronous memory

• Host port interface

• 2 multi-channel buffered serial ports

• 4 DMA channels

To shorten development time, the evaluation module (EVM) for the TMS320C6XXX family was chosen as the controller board for the system. Texas Instruments builds the EVM and it includes the following features:

EVM module:

• 1 bank of 64K x 32bit 133 MHz SBSRAM memory

• 2 banks of 1M x 32bit 100 MHz SDRAM memory

• Connection to the memory bus via daughter card connector (allows up to 3M more memory)

• Connection to the peripheral interface bus via daughter card connector

The daughter card connectors on the EVM allow third party expansion boards to be easily plugged into the system.

5.5.2 Control Peripheral Daughter Card

A Signalware, Inc. AED-106 daughter card was chosen to provide the necessary peripherals for the control system. Figure 2.13 gives a diagram of the EVM board and the AED-106 and their connections to each other.

TMS320C6701 EVM   AED-106 Daughter Card

Figure 21. Block diagram of EVM and AED-106 boards.

The AED-106 board has the following features:

• Xilinx Virtex XCV300 series FPGA for interfacing the memory and peripheral bus from the DSP to peripherals for control applications.

• 2 banks of 512k x 8bit Flash memory for boot loading and program storage.

• 4 THS1206 4 input 12 bit A/D converters, allowing 6 MSPS each.

• High speed (70MHz) amplifiers at the input of each A/D channel for use in a anti-aliasing filter.

• 24 configurable digital I/O lines.

The FPGA on the daughter card allows good flexibility in the controller design. All of the 16 A/D converters are buffered in the FPGA to allow for proper synchronization between the sampling and the transfer to the DSP memory. The FPGA also provides a very flexible digital I/O configuration. In this design, as discussed in Chapter 4, several of the digital I/O pins on the daughter card were used as the PWM channels for the power device gate signals to the inverter. Another digital I/O pin was set up as a PWM channel and passed through an external low pass filter to provide a D/A converter for the control signal to the DC/DC converter control chip. All of the fault signals from the inverter gate drives are OR'ed together to and fed back to one of the digital I/O pins. Another pin is used for the same purpose for the DC/DC converter. Two digital I/O pins are used to provide reset signals to the gate drives on each of the power stages.

5.5.3   A/D Converter Signal Conditioning

Texas Instruments THS1206 A/D converters are used on the daughter card. These A/D converters have a maximum sampling rate of 6Msamples/sec. at 12-bit resolution. There are 4 A/D chips and each chip has 4 channels that are sampled simultaneously, then the values are converted sequentially by a muxed 12-bit A/D converter and stored in a local buffer before being transferred over a parallel bus to a FIFO buffer in the FPGA. The input voltage range for the A/D converter channels is –1 V to +1 V.

All of the analog signals used in the control system come from either LEM voltage or current sensors. The LEM LV-25, 10-500Vrms voltage sensor is used for all voltage measurements and the LEM LA-55, 50Arms current sensor is used for all current measurements. Additional channels of the A/D converters are reserved for the Airak, Inc. fiber optic current sensors. The output of the LEM sensors is a current in the 10mA range that is proportional to the measured variable. The conditioning circuits that were designed to interface the LEM sensors to the A/D converters provide a burden resistor to convert the current signal from the sensor to a voltage signal within the input range of the A/D converters. A picture of the conditioning circuits is shown in Figure 22. Example schematics of the conditioning circuits are shown in Figure 23.
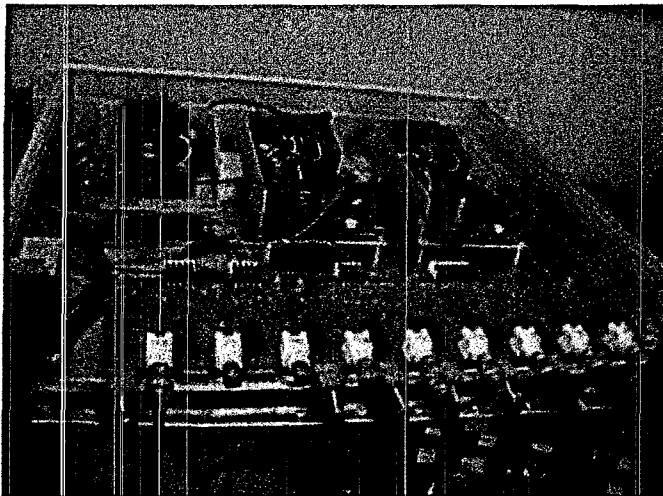
Figure 22. Analog signal conditioning circuits.

The first circuit schematic is used to measure AC quantities and does not offset the measured signal from zero. To fully utilize the input range of the A/D converters, the DC quantities are offset to –1V as in the second schematic in Figure 23. In the signal conditioning circuits an instrumentation amplifier is used to make a differential measurement on the burden resistor. Two LM347 op-amps are used to provide offset for the DC circuits and to allow adjustment of the offset to zero in the AC circuits and to –1V in the DC circuits with a potentiometer. A final op-amp is used in each circuit for a first order low pass, anti-aliasing filter for the A/D channels. The cutoff of the low pass filters is set at one half of the sampling frequency of the A/D channels. After the signal passes through the anti-aliasing filter, it is connected back to the daughter card through a National Instruments breakout box. The breakout box also provides the connections for the digital I/O.
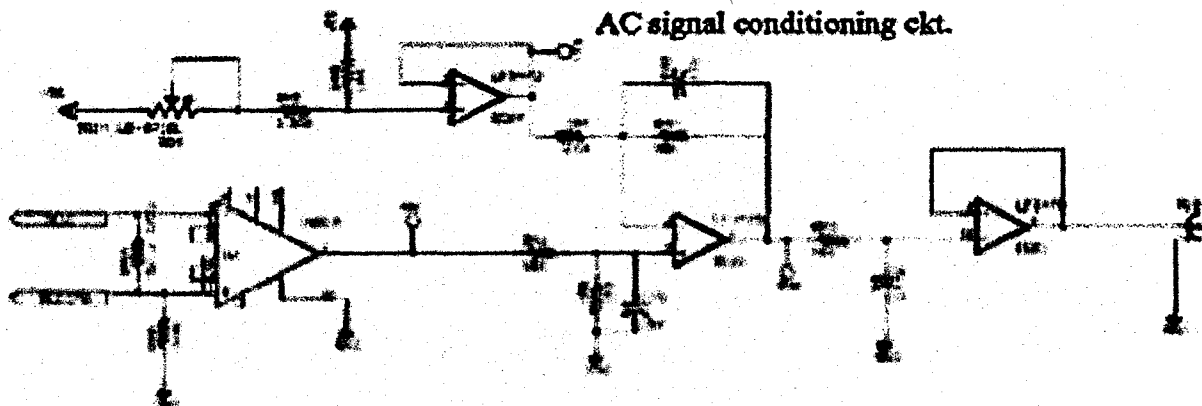

Figure 23. Signal conditioning circuit schematics.

5.5.4 Digital Interface

The digital I/O on the controller are interfaced to the system through a National Instruments breakout box and then through the interface board. The cable from the breakout box plugs into the large connector on the interface board and the signals are split up to be sent to the inverter/active filter power stage through J2 and the DC/DC converter through J3 and J4. A second order low-pass filter is placed in series with the PWM signal that controls the duty cycle to the DC/DC converter to form a D/A converter because the controller on the DC/DC converter requires a 0.5V to 3.5V signal for the duty cycle control.

5.6 CONCLUSIONS

This section described the hardware that was designed for the system including the power stages and the controller. The DC/DC converter and the PV array were designed and built, but due to a design oversight discussed in detail in Task 4 they were not included in the system that was built and tested.

6. Task 4: Integrate and test the electro-optical and power electronic subsystems (join Tasks 2 and 3).

6.1 PV ARRAY MODEL

One of the mistakes made in this work was an improper simplifying assumption about the behavior of the PV array. It was assumed that the behavior would be similar to an ideal voltage source in series with a resistor, and the original controller design was based on that assumption. Later in the design, a more accurate model of the PV array was developed and used in the controller simulations.

A more accurate model of the PV array was later developed using the datasheet information for the Siemens PV modules that were to be used in the system. The model[9] allows the module manufacturers data to be used to create a model of the entire array to be used in simulations. The simulation model was implemented as a Mast file for use in the Saber simulation package. An example simulation of the PV array model is shown in Figure 24 where a resistive load is swept from a low value to close to a short circuit condition. The model becomes numerically unstable as the load approaches a short circuit and therefore the model cannot be used for simul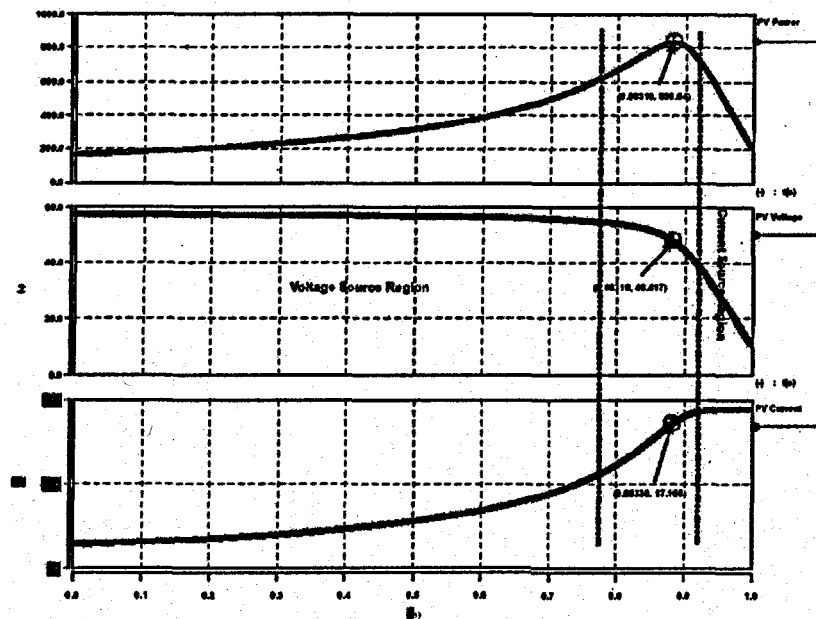ations that may require short circuit conditions. The waveforms in Figure 24 show the voltage source region, the current source region and the transition region where the maximum power point exists. As the power profile shows, the maximum power of the model is 8% lower than the rated power of the actual PV array, but the basic behavior of the array is present.

Figure 24. Load sweep simulation of the PV array model.

6.2 DC/DC CONVERTER MODEL AND CONTROLLER

At the beginning of the design process an incorrect assumption was made about the behavior of the PV array as discussed previously and the DC/DC converter control design was based on that assumption. The

[9] A. D. Hansen, P. Sørensen, L. H. Hansen, and H Bindner, "Models for a Stand-alone PV System," Wind Energy and Atmospheric Physics Department, Electrical Design and Control Group, Risø National Laboratory, Roskilde, Denmark, December 2000

control loop for the front end DC-DC converter was developed using Saber. The model for the converter was built in Saber based on the averaged switch model proposed by Tsai[10]. Initial simulations of the converter showed that in the operating range available from the PV array, the converter would always operate in the discontinuous conductions mode.

Because the DC/DC converter had already been designed when the problem with the model was discovered, the decision was made to not implement the PV array and DC/DC converter in hardware. More work needs to be done to either redesign the DC/DC converter or add a buffer between the PV array and the DC/DC converter to allow the DC/DC converter voltage loop bandwidth to remain high enough for the proposed control scheme to work.

---

[10] F. Tsai, "Small-Signal and Transient Analysis of a Zero-Voltage-Switched, Phase-Controlled PWM Converter Using Averaged Switch Model," IEEE Transactions on Industry Applications, Vol. 29, No. 3, May/June 1993.

7. Task 5: Compare/contrast advantages of fiber optic sensing configuration over conventional sensing and control loop methodologies

7.1 COMPETITIVE TRANSDUCER TECHNOLOGY COMPARISON MATRIX

Table 3. Comparison of Three Types of Magnetic Field or Current Measurement Technologies

Technology	Bandwidth	Simultaneous AC & DC Measurements	Voltage Range	Dynamic Range	Accuracy	Intrinsically Isolated	Install on Energized Line	Size	Weight	Reliability	Price
Airak's Optical Transducer	DC - >30 MHz	Yes	<19.2KV	> 100 dB	High	Yes	Yes	Constant, Independent of Voltage or Current Range	Constant, Independent of Voltage or Current Range	Extremely High	Constant, Independent of Voltage or Current Range
Wire-wound	Few Hz – 100 KHz	No	<1.2 MV	< 60 dB	Medium	No	No	Increases Dramatically as Voltage Increases	Increases as Either Voltage or Current Increases	Decreases as Voltage Increases due to Oil Insulation	Increases Roughly as the Square of the Voltage over 1KV
Hall-effect	DC – 10 KHz -or- Few Hz – 250 KHz	Depends	< 2KV	< 80 dB	High	No	No	Increases as Voltage Increases	Increases as Voltage Increases	Decreases as Voltage Increases	Increases Linearly as Voltage Increases

Bandwidth. Table 3 provides an overview of technologies that directly compete with Airak's optical transducer technology. As established in Section 9, Airak's transducer has a bandwidth in excess of 30 MHz, and by tailoring the Faraday crystal composition this response can be made at least as high as 700 MHz. Wire-wound technologies suffer two limitations: as they get larger core losses increase and frequency response decreases. For wire-wound transducers in the 1000-A range the maximum frequency response is typically less than 25 kHz, and this will decrease rapidly as the size of the transducer increases. Hall-effect transducers, while exhibiting higher frequency response, suffer in that devices capable of measuring DC magnetic fields or DC current typically are restricted to less than 10 kHz response and higher-end Hall-effect transducers capable of monitoring AC signals have an upper bandwidth limit of 250 kHz.

Simultaneous AC & DC Measurements. With respect to AC and DC measurements, only Airak's transducer is capable of simultaneously measuring a steady-state DC offset in magnetic field or current and reporting an AC magnetic field or current at the bandwidths listed. Any DC present in a measurement signal will cause a wire-wound transducers' core to saturate, which will introduce huge measurement errors (if not render the measurement useless).

Voltage Range. Airak's transducer, as shown in Figure 2, has been tested through 6 kV and is capable of operating at least through 19.2 kV with no additional requirements for insulation, isolation, or cooling. Although wire-wound transducers are used in electrical transmission applications as large as 1.2 MV, this is only achievable with oil-filled assemblies. Hall-effect transducers are typically less than 2 kV for devices in the 3- to 3000-A range, largely due to their isolation and insulation requirements.

Dynamic Range. The dynamic range of Airak's transducer is extremely high, due largely to the optical nature of the device. Advanced signal processing methods, as well as advanced optical support configurations can drive the dynamic range in excess of 120 dB (power). In contrast, wire-wound transducers are typically limited to 60 dB (power) total dynamic range, due to effects such as self-heating and saturation. Hall-effect devices have a larger dynamic range than their wire-wound counterparts, due in part to advanced signal processing as well as the all-semiconductor structure, but they still fall short of optical methods.

Accuracy. The accuracy of Airak's transducer and of traditional Hall-effect devices is comparable, due largely to advanced signal processing techniques. Conventional wire-wound technologies, especially in higher voltages, suffer due to the same effects that limit their dynamic range (see Appendix C).

Intrinsically Isolated. The all-fiber interconnection of Airak's transducer provides a natural separation between the conductor being monitored and the equipment performing the measuring. The result is an extremely safe measurement device, especially compared to the other technologies. This intrinsic isolation is far different than wire-wound or Hall-effect devices, which typically require substantial insulation as voltage increases.

Install on Energized Line. The quick connect/disconnect feature of Airak's transducer, coupled with the intrinsic isolation, allow it to be directly connected to energized lines, relatively independent of the power flowing through the line. Neither wire-wound technologies nor Hall-effect technologies can be connected to energized lines due to safety and potential grounding problems.

Size. As previously established, Airak's transducer is 35 mm in length and 12.7 mm in diameter, independent of the field being monitored or the voltage on the line to which it is attached. Neither the wire-wound nor Hall-effect technologies can maintain a constant size as system power levels change due to increased demands concerning full-scale measurement range, isolation, and safety.

Weight. The weight of Airak's transducer is fixed at 28 grams, completely independent of the field being monitored or the voltage on the line to which it is attached. Again, neither wire-wound nor Hall-effect technologies can maintain a constant weight as system power levels change because of isolation and safety requirements.

Reliability. The all-optical nature of Airak's technology improves overall transducer reliability. Wire-wound transducers, especially those that are used at high voltages, typically contain insulating oils that break down over time, reducing their mean-time-between-failure. Hall-effect transducers are subject to stress fatigue, especially in higher voltage environments, causing a significant decrease in reliability for applications above 1 kV.

Price. The price of the Airak transducer is constant even when current magnitude or system voltage level increases. The cost of wire-wound and Hall-effect technologies increases rapidly as system voltage levels increase.

8. Task 6: Deliver the APCS testbed to NSWCCD for independent performance validation and PEBB interfacing.

Over the course of the program it was determined that NSWCCD was not equipped nor were they funded to evaluate the performance of the APCS testbed. Despite this, NSWCCD was able to secure partial funding to evaluate the optical current sensor. As a result, a complete FOECT sensor system that was developed on the APCS program was delivered to NSWCCD for evaluation in September 2002. The technology has been proven and a letter of support from NSWCCD follows:

DEPARTMENT OF THE NAVY
NAVAL SURFACE WARFARE CENTER
CARDEROCK DIVISION

NAVAL SHIP SYSTEMS
ENGINEERING STATION
5001 S. BROAD STREET
PHILADHPHIA PA 19112-1403

From: Head, Machinery Research Department (9B), Naval Surface Warfare Center
To: Mr. Paul Grems Duncan, President
Airak, Inc.
9058 Euclid Avenue
Manassas, Virginia 20110-5308

Subj: Potential for Carderock Division Partnering with Airak

Dear Mr. Duncan:

The Machinery Research and Engineering Directorate, Naval Surface Warfare Center Carderock Division (NSWCCD) is the United States Navy's laboratory for the development of ship machinery systems and the in-service engineering to support these systems in the Fleet. With the development of the more electric Navy shipboard electrical monitoring requirements will increase, and NSWCCD is constantly seeking innovative approaches to solve this challenging problem.

Airak has proposed to develop low-cost optical sensors that monitor current for fast detection of electrical faults in shipboard electrical power distribution systems. Your development of low-cost optical sensors that could potentially meet the bandwidth and electrical isolation requirements of this demanding environment and the associated transducer system has potential for Navy application.

NSWCCD can provide support of Airak optical sensor developments under a work for private parties agreement. NSWCCD participates in these agreements to support technical capabilities essential for the Navy, to support dual use and technology transfer opportunities, reduce total ownership cost for the Department of Defense, increase national competitiveness, and support regional economic development. If Airak chooses, NSWCCD is prepared to discuss the process in greater detail. NSWCCD could provide Airak assistance through the use of test equipment, test facilities, and engineering expertise to provide guidance on methods to ruggidize transducer and electro-optical systems for the rigors of the shipboard environment.

NSWCCD wishes Airak, Inc. success with their research and commercialization efforts.

Sincerely,

E.M. Golda

9. Task 7: Sol-gel thin-film materials development and characterization.

9.1 IMPORTANCE OF THE RESEARCH

As power electronics continue to decrease in size and cost, the need for small, low-cost, high-performance, noise-immune current sensors dramatically increases. It is generally believed that the next generation of hybrid Integrated Power Electronics Modules (IPEMs) will introduce many new technologies such as active thermal control, integrated gate drivers with active di/dt and dv/dt control and integrated current sensors. The feedback controls from current sensors make possible to generate risk-free power modules. Engineers are investigating various current sensing technologies intensively to serve as candidates for integration into the new generation of power electronics module. The shunt resistor, though small in size and cheap in fabrication price, requires Galvanic isolation and have large insertion loss, which can be costly in long run. Current transformers need iron cores and are largely affected by EMI noise, which make them an unlikely candidate for integration. These two limitations are also applied to Hall-effect sensors. Though one may remove the iron cores from the Hall effect-based sensor tips, their relatively low AC bandwidth (10 to 200 KHz)[11] could be another disadvantage for the applications in power modules. Coreless, wireless magnetoresistive-based current sensors have a high-speed working characterization[12] and may offer a performance superior to that of standard open-loop and closed-loop Hall effect-based current sensors, so they could be one of the candidates of integrated current sensors for the next generation of power modules. But they have limitations in large noise environments, less accuracy, exhibit non-linearity and non-zero offsets, as well as saturation and hysteresis.

Is it possible to design and develop integrated current sensor using magneto-optical sensing techniques? If possible, how good are the magneto-optical sensors as a candidate in the next generation of IPEMs, especially when compared with the other techniques in each specific characterization? In this research report, we will leverage our lessons learned from past research efforts with our existing research results to contribute in replying these questions with help of the recent advances in materials, optics, MEMS, and semiconductor processing.

There are many concerns that need to be investigated if magneto-optical current sensors are to be used in integrated power modules. The key parameters are (1) sensitivity, (2) workable bandwidth, and (3) accuracy. Each will be discussed:

9.2 SENSITIVITY OF MAGNETO-OPTICAL SENSORS

For a magneto-optical rotation material in a basic polarimetric detection scheme as shown in Figure 25, when the rotation angle is small (which is the usual case in a magneto-optical sensor application) we have the signal changes from the detector:
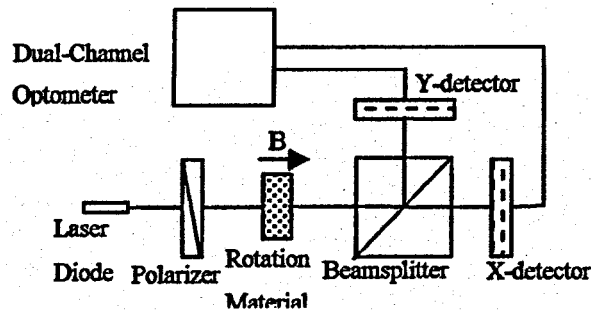

Figure 25. Schematic diagram of system setup for determining magneto-optical rotation.

$$\Delta I = I_0 * V(\lambda) * \Delta B * l * e^{-A(\lambda)l} * R_s(\lambda) * R_d(\lambda) * C$$

---

[11] J. Sedgwick, W. R. Michalson, and R. Ludwig, "Design of a digital gauss meter for precision magnetic field measurement", IEEE Transactions on Instrumentation and Measurement, 47 (1998) pp972-977

[12] S.E. Russek, J.O. Oti, S. Kaka, and E.Y. Chen, "High-speed characterization of submicrometer giant magnetoresistive devices", J. Appl. Phys., 85 (8) pp4773-4775 1999

where I_0 is the intensity of photo-diode module laser source, V is the Verdet constant of the sensing material, A the absorption coefficient of the sensing material, R_s the responding of the polarizing cube beamsplitter and/or the polarizers, R_d the responding of the photo-diode detector, and C the other signal attenuation/amplification in the optical path. From the previous equation, when $A*l = 1$, we have the maximum signal changes from the detector:

$$\Delta I_{max} = I_0 * \frac{V(\lambda)}{A(\lambda)} * \Delta B * R_s(\lambda) * R_d(\lambda) * 0.368C$$

From this equation we know that $M(\lambda) = V/A(\lambda)$ is an important parameter to indicate the maximum sensitivity of a given material and is called magneto-optical figure of merit of the material. The larger $M(\lambda)$ is, the larger the maximum signal changes we can get from the detector, as long as we can optimize the length of the sensing material along the field direction to be $l = 1/A$. Therefore the determination of $M(\lambda)$ is crucial for selection of the operating wavelength and enhancement of the sensitivity of the sensor.

9.3 WORKABLE BANDWIDTH

The working bandwidth is another important concern in applications of the magneto-optical current sensor because a high frequency switching power-module could need a response speed up to several MHz. The response behavior of the magneto-optical rotation materials of garnets depends on domain wall damping or domain wall resonance in the same way as the magnetic susceptibility. Theory and experiment show that the speed of operation is limited by relaxation of resonance effects to upper frequencies between 10^6 to 10^9 Hz. As examples, two $(BiTb)_3(FeGa)_5O_{12}$ films grown by standard liquid epitaxy techniques have the 3 dB roll-off frequencies of 8×10^6 and 7×10^5 Hz, respectively, as shown in Figure 26.[13] Theoretically, the roll-off frequency should be the highest working speed point of a magneto-optical sensor made use of the sensing material. For the sensing materials with large damping, the cut-off frequency has a relationship of

$$F_{max} \propto M_s^2 / (K^{3/4} l^{1/2} d)$$

where M_s is the saturation magnetization, K is the uniaxial anisotropy energy, l is the thickness, and d is the damping of the sensing material. From this equation it is obvious that the cut-off frequencies can be obtained by maximizing the magnetization and by minimizing the material thickness, the uniaxial anisotropy, and the damping. This could provide us some useful prediction for selecting rare earth ions doped to the garnet composition. For example, from the response speed point of view, terbium is not a good choice because it has large damping though it is the best choice for temperature stability and therefore a compromise must be reached for our realistic application. Since these requirements often show conflict with those for higher sensitivity, a compromise must be reached for each potential application.

[13] R. Wolfe, E. M. Grorgy, R. A. Lieberman, V. J. Fratello, S. J. Licht, M. N. Detter and G. W. Day, "High frequency magnetic field sensors based on the Faraday effect in garnet thick films", Appl. Phys. Lett., 60(17) 2047 (1992).

Page 30

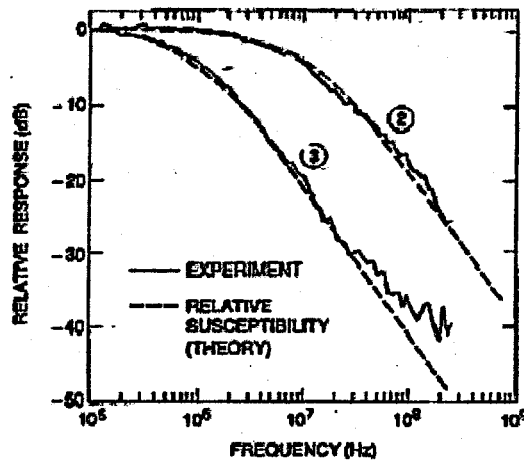*Figure 26. Optical response vs frequency of applied field for two (BiTb)3(FeGa)5O12 films 2 and 3.*

9.4 ACCURACY

Among several parameters restrict absolute accuracy of an integrated magneto-optical sensor, the non-zero temperature sensitivity is the most concerned one because power electronic devices are heat-dense, especially as power density increases within an integrated power module. The magnetic field/current sensor must be able to operate over a specified temperature range. Unfortunately, the Faraday rotation of the rare-earth iron garnets is not constant over this temperature range. The temperature coefficient of Faraday rotation in bismuth-doped compositions is typically 0.06 to 0.08 degree/°C compared to 0.04 degree/°C in YIG.

The Faraday rotation of an iron garnet is given by

$$\Theta_F = C(\lambda)M_c(T) + D(\lambda)M_d(T) + A(\lambda)M_a(T)$$

where $C(\lambda)$, $D(\lambda)$ and $A(\lambda)$ are the wavelength-dependent magneto-optic coefficients, respectively, of the c (dodecahedral), d (tetrahedral) and a (octahedral) sublattices. These coefficients contain a small magnetic term and an electric dipole term that is significantly affected by Bi substitution through superexchange and spin-orbit interactions. $M_c(T)$, $M_d(T)$, and $M_a(T)$ are temperature-dependent saturation magnetizations of the sublattices. The first idea for decreasing the high temperature dependence of the Bi-induced Faraday rotation is to adjust the rest of the constituents of the garnet to compensate for the large temperature dependence of the Bi-induced component. However, the Bi-induced component is so strong that the other constituents have only a minor effect. The one additive atom that makes a slight difference is Tb (terbium). The heavy rare earths such as Tb have their magnetic moment aligned antiferromagnetically to the net iron lattice moment, with a weak coupling to the iron sublattices (d and a) that causes the c sublattice magnetization to vary sharply, approximately as 1/T. This results in a large negative temperature coefficient of $M_c(T)$ in the region of interest. Tb is an unusual element, as it has a large negative $C(\lambda)$, so the coupling of the c lattice magnetization to the Faraday rotation is significant. The entire Faraday rotation of the terbium iron garnet (TbIG) arises from the c lattice contribution. TbIG has both a Faraday rotation of opposite sign to that of the heavily Bi-doped iron garnets and high temperature dependence.[14] When these two effects are combined, the Tb incorporation reduces the net Faraday rotation, but more so at low temperatures, reducing the effective temperature coefficient of the Faraday rotation in the material. The temperature coefficient of the Faraday rotation is dependent on the ratio of Bi to Tb. It is possible to obtain a material with zero temperature coefficients, but it requires a low Bi concentration and hence results in a low specific rotation.[15] Taking into account these results, (BiTb)3(FeGa)5O3 is one of good candidates to optimize the Bi/Tb ratio and obtain a reduction in the temperature coefficient as compared to compositions with no Tb.

---

[14] Kanada, O., Minemoto, H., and Ishizuka S. "Mixed rare-earth iron garnet (TbY)IG for magnetic field sensors" J. Appl. Phys. 61, p. 3268, 1987.

[15] Honda, Y., Ishikawa, T., and Hibiya T. "Temperature dependence of Faraday rotation for Bi-substituted Tb iron garnet films" J. Magn. Soc. Jpn. 11, p.361, 1987.

In order to be a viable sensor, magneto-optical materials with larger Verdet constants, lower absorption and larger figures of merit are required in order to enhance the Faraday rotation response. Larger Verdet constants increase the sensitivity of rotation material, permits thinner sensor materials and therefore is crucial for miniaturization of the probes and their integration. Lower absorption implies the requirement of less optical power, which lowers the costs. Rare-earth doped yttrium ion garnets (YIGs) usually have large Verdet constants and large figures of merit and they can be prepared on silicon (Si) or gadolinium gallium garnet (GGG) substrates by a sol-gel processing.[16,17,18]

In our opinion, the sol-gel approach is an economic and promising way to fabricate the probes for on-chip sensing application since a considerable body of experimental work, including experience in our lab, has shown that doped YIG films can be successfully applied to Si or GGG substrates. Sol-gel processing usually includes two steps: first is preparation of sol followed by coating and annealing the film on the substrates.

Preparation of Sol:

The processing of Bi:YIG films requires careful control of many parameters to produce both an optically and mechanically viable sensing material. Intrinsic to the composition is the solvent concentration of the starting sol, the control of solution pH, variation of Bi or Al substitution, and the viscosity control by heating time and temperature. The solvent concentration of the starting sol will affect the resultant coating because the amount of shrinkage during drying and the thickness of coating affect the film quality. Acidity or pH affects the quality of the sol obtained after heating and also the coating after firing. A low pH makes the solution susceptible to precipitation of uncomplex ions while a higher pH keeps the ions in the complex states. The amount of Bi or Al substitution will determine the match with the GGG or Si substrates while keeping the desired properties at acceptable levels. Heating can control the viscosity of the sol and induce gelation. Viscosity control is important as it affects the thickness and uniformity of the coated films whether by spin coating or dipping.
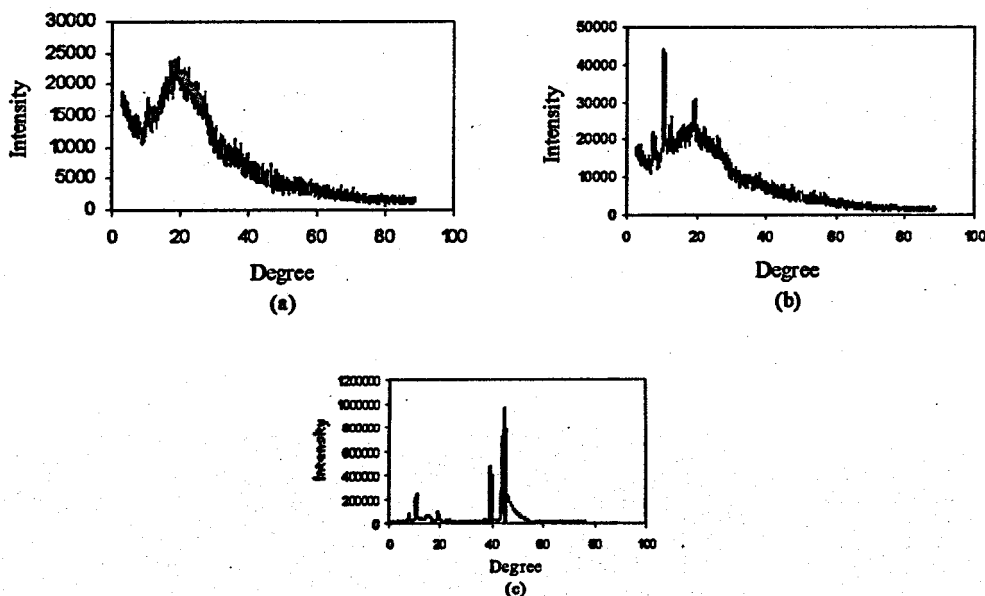

Figure 27. X-ray diffraction (XRD) results from (a) glass substrate without sol-gel film, (b) glass substrate with a film, and (c) a GGG substrate without sol-gel film.

[16] Koji Matsumoto, Satoshi Sasaki, Yasunori Yamanobe, Kazuhiro Yamaguchi, Toshitaka Fujii, and Yousuke Asahara, "Bismuth- and aluminum-substituted YIG single-crystal films on modified gadolinium gallium garnet single-crystal substrates", J. Appl. Phys., 70 (3) 1991, pp1624-1629.

[17] T. Tsuchiya, T. Sei, and H. Kanka, "Sol-gel preparation of YIG (Y$_3$Fe$_5$O$_{12}$) thin film showing opto-magnetic effect", J. of Non-crystalline solids" 147&148 (1992) pp463-466.

[18] Eiji Kato, Tadanori Sei, and Toshio Tsuchiya, "Preparation of highly oriented thin film exhibiting a magneto-optical effect in Bi, Al doped YIG", J. of the Ceramic Society of Japan, 102 (9) 1994, pp818-821

Coating and annealing of films on substrates:

Both spinning and dipping can be used to produce coatings. Spinning provides thinner coatings over that of dipping. Drying and annealing are the final steps in the fabrication of films on substrates. In one of our experiments, a sol solvent was obtained following the formula $Bi_{1.5}Y_{1.5}Fe_5O_{12}$ with nitrates of the metal ions. To improve sol-gel reaction, ethylene glycol and ethyl acethyl acetate were mixed together with the selected proportion. To ensure crack-free and strong adherent thin films, the substrates were ultrasonically cleaned in acetone for one hour, and then, soaked in diluted nitrate acid with ultrasonic shaking for another hour. Finally, the substrates were washed with de-ion water and dried under a drying hood.

After spinning the sol solution on the treated substrates, the films were heated to 500 °C slowly to drive off the organic solvents and NO_x. The dried films were then heated rapidly to about 700 °C to avoid maghemite precipitating out to form hematite at around 650 °C before densification and crystallization into the garnet structure. The later part of the heating process has to be controlled carefully in order to ensure Bi substitution and crystallization into the Garnet structure. Smooth, crack-free films were obtained on GGG, Si, and glass substrates.

X-ray diffraction (XRD) results:

The crystalline structure of sol-gel films was checked by a Scintag XDS2000 Automated X-ray diffractometer (Cu $K_{\alpha1}$, radiation $\lambda = 1.54060Å$). For comparison, diffraction data on the substrates without the coated films were also collected as shown in Figure 27. The x-ray diffraction results are from (a) glass substrate without sol-gel film, (b) glass substrate with a film, and (c) a GGG substrate without sol-gel film. Because the peak near 11 degrees in (b) appears in (c), we can conclude that the film crystal structure is similar to that of the garnet. However, in this attempt, when the magneto-optical response of the thin films was checked using the optical setup, no conclusive data were obtained. After predicting the response calculation, it was believed that the films were too thin (less than 0.1 micron) to produce any detectable Faraday rotation.

Scanning electron microcopy (SEM) results:

In another research attempt, thin film formation via sol-gel processing was begun with mixing of precursors. A liquid solution was spun-coated upon a substrate following the mixing of the components. Spin rate and time were varied to determine optimum parameters to prepare a film that would remain uniform and crack free upon completion of processing. Multiple coating was performed to increase the thickness of the deposited films. Finally, heating the material in an attempt to form the desired crystalline material was performed. Once the spin coating was completed the sample was placed in a furnace and heated to a temperature exceeding the Curie temperature of the yttrium iron oxide – this induced crystallization. The film surfaces were checked using a SEM and representative results are shown in Figure 28. Low temperature (150°C) treated films were exposed to lower processing stresses as well as possessing solvent thereby allowing easier relaxation to occur. This explained the smooth surface features seen in Figure 28(a) with respect to porous surface features in Figure 28(b).

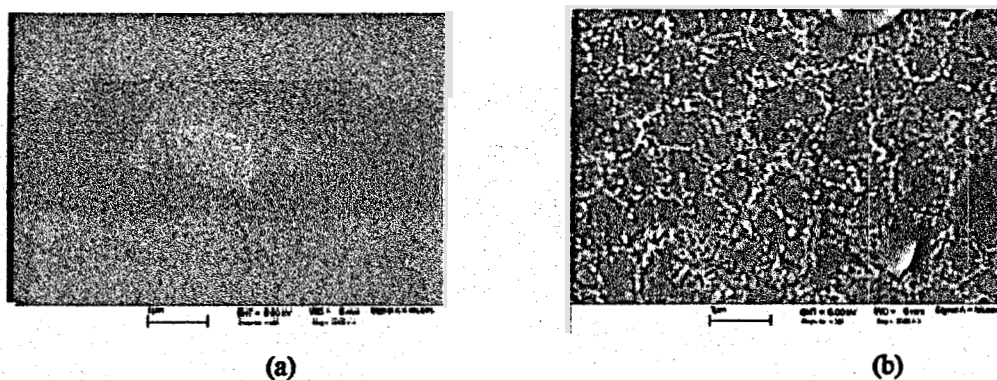(a)   (b)

Figure 28. SEM showing smooth surface of a low temperature (150°C) treated film (a) and porous featured surface of a high temperature (900°C) treated film (b).

Our experimental work is preliminary. For further systematic study to grow high quality thin films, the following focus is presented:

- The issue of film cracking needs to be further addressed through variations in the concentration of the sol.

- Variation in the initial pH values need to be studied to determine pH levels at which films of acceptable quality can be obtained.

- The amount of Bi or Al substitution need to be determined for the best crystal lattice match with the intended GGG and Si substrates while keeping the desired properties at acceptable levels.

- The effect of spin coating speed and drying time on the thickness and quality of the films produced need to be determined.

- More systematic analyses of the effects of drying and annealing profiles on the characteristics of the crystallized films.

9.5   CHARACTERIZATION OF GARNET CRYSTALS
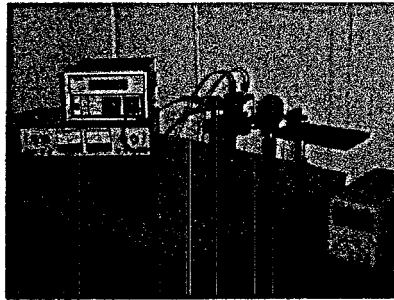
Figure 29. Optical bench setup for determination of magneto-optical rotation.

Theoretical basis:

In a dual channel-polarimetric detection scheme corresponding to the optical bench setup in Figure 29 and the vector representation in Figure 30, suppose that the incoming electric vector of the laser beam $\vec{E_0}$ makes an angle of α with the x-direction photodetector. After passing through the rotation material, the electric vector $\vec{E}$ of the outgoing laser beam is rotated by an angle θ with respect to the original vector $\vec{E_0}$. Assume that the absorption coefficient of the Faraday material is A, thickness of the material is l, we have:

$$E_{0x} = E_0 \cos(\alpha)$$
$$E_{0y} = E_0 \sin(\alpha)$$
$$E_x = E_0 \cos(\alpha + \theta)$$
$$E_y = E_0 \sin(\alpha + \theta)$$

$$E'_{0x} = E'_0 \cos(\alpha) = E_0 \cos(\alpha)e^{-Al/2}$$
$$E'_{0y} = E'_0 \sin(\alpha) = E_0 \sin(\alpha)e^{-Al/2}$$
$$E'_x = E_x e^{-Al/2} = E_0 \cos(\alpha + \theta)e^{-Al/2}$$
$$E'_y = E_y e^{-Al/2} = E_0 \sin(\alpha + \theta)e^{-Al/2}$$
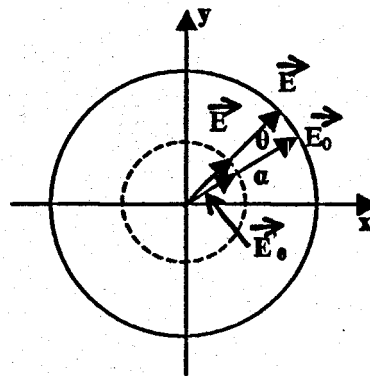
Figure 30. Faraday rotation and absorption.

Since photodetectors only detect the light intensity, which is the square of the electrical field vector, we have the signal from the x-detector:

$$|I_{0x}| \propto |E_{0x}|^2 \,, \ |I_x| \propto |E_x|^2 \,, \text{ and}$$

Signal from the y-detector:

$$|I_{0y}| \propto |E_{0y}|^2 \,, \ |I_y| \propto |E_y|^2$$

If there is no absorption by the material, signal changes detected by the x- and y-detectors are:

$$\Delta I_x = I_x - I_{0x} \propto E_x^2 - E_{0x}^2 = E_0^2 \cos^2(\alpha + \theta) - E_0^2 \cos^2(\alpha) \propto -\sin(2\alpha + \theta)\sin\theta$$

$$\Delta I_y = I_y - I_{0y} \propto E_y^2 - E_{0y}^2 = E_0^2 \sin^2(\alpha + \theta) - E_0^2 \sin^2(\alpha) \propto \sin(2\alpha + \theta)\sin\theta$$

Since the material absorbs light, the actual signal changes detected by the two detectors are:

$$\Delta I'_x = I'_x - I'_{0x} \propto -\sin(2\alpha + \theta)\sin\theta \cdot e^{-Al}$$

$$\Delta I'_y = I'_y - I'_{0y} \propto \sin(2\alpha + \theta)\sin\theta \cdot e^{-Al}$$

If the Verdet constant of the rotation material is V, the rotation angle will be:

$$\theta = VBl$$

Insert the above equation into the two equations for signal changes with absorption, we have:

$$\Delta I'_x \propto -\sin(2\alpha + VBl)\sin(VBl) \cdot e^{-Al}$$

$$\Delta I'_y \propto \sin(2\alpha + VBl)\sin(VBl) \cdot e^{-Al}$$

If we set $\alpha = 45°$, and assume that $\theta = VBl$ is very small compared with 2α (90°), then

$$\Delta I'_x \propto -\cos(VBl)\sin(VBl) \cdot e^{-Al} = -\frac{1}{2}\sin(2VBl) \cdot e^{-Al} \cong -VBl \cdot e^{-Al}$$

$$\Delta I'_y \propto \cos(VBl)\sin(VBl) \cdot e^{-Al} = \frac{1}{2}\sin(2VBl) \cdot e^{-Al} \cong VBl \cdot e^{-Al}$$

Therefore, the signal changes, in both detectors, reach their maximum values simultaneously when the thickness of the rotation material is the reciprocal of its absorption coefficient, i.e.,

$$l = 1/A$$

The maximum values are proportional to V/A:

$$(\Delta I'_x)_{max} \propto -V/A$$
$$(\Delta I'_y)_{max} \propto V/A$$

In the realistic applications, $M(\lambda) \equiv V(\lambda)/A(\lambda)$ for a given rotation material and is therefore very important for the maximum sensitivity that could be attained. This is known as figure of merit of the material.

When determining the Verdet constant, after we find relative values of $E'_{0x}, E'_{0y}, E'_x, E'_y$ from the raw data of $I'_{0x}, I'_{0y}, I'_x, I'_y$, we use the equations of:

$$\frac{E'_x - E'_{0x}}{E'_{0y}} = \frac{\cos(\alpha + \theta) - \cos(\alpha)}{\sin(\alpha)} = \frac{-2 \cdot \sin(\alpha + \frac{\theta}{2}) \cdot \sin(\frac{\theta}{2})}{\sin(\alpha)} \cong -\theta$$

$$\frac{E'_y - E'_{0y}}{E'_{0x}} = \frac{\sin(\alpha + \theta) - \sin(\alpha)}{\cos(\alpha)} = \frac{2 \cdot \cos(\alpha + \frac{\theta}{2}) \cdot \sin(\frac{\theta}{2})}{\cos(\alpha)} \cong \theta$$

to determine θ. Finally the Verdet constant of the sensing material can be calculated from

$$V = \theta / Bl$$

Experimental results:

Two types of crystals were analyzed. American-grown crystals from Deltronic Crystal Industries of Dover, NJ and Russian crystals provided by MODIS of Reston, Virginia were characterized by a setup as shown in Figure 29. The American $(BiYbTb)_3Fe_5O_{12}$ crystal is grown by LPE and it has a Verdet constant about 5.33°/(G-cm) at 780 nm. Its absorption coefficient at this wavelength is about 73.6 cm^{-1}, so it has a figure of merit of 0.0724°/G at 780 nm. While for shorter wavelengths such as 633 nm and 543 nm, its Verdet constants are undetectable using the setup because the absorption coefficient is too high to detect a signal. The Russian crystal is most likely a diluted bismuth doped YIG and its Verdet constants are shown in Figure 31 at wavelengths of 543 nm, 633 nm and 780nm. Its absorption coefficients are shown in Figure 32 and figures of merit are shown in Figure 33.
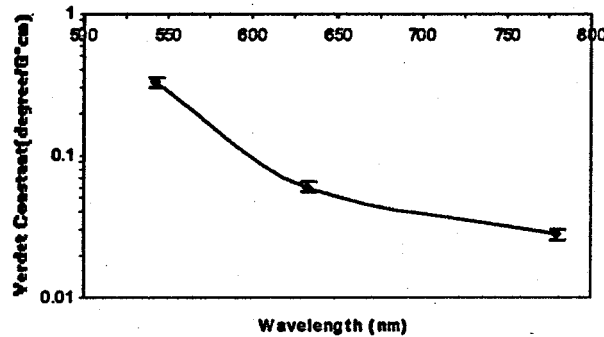
Figure 31. Verdet constant of the Russian crystal.
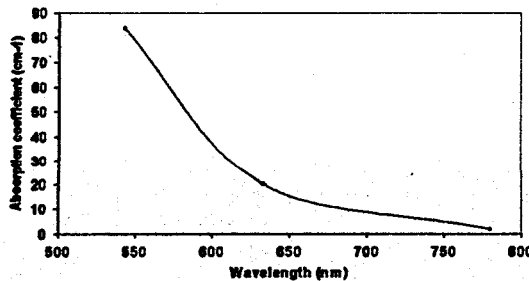
Figure 32. Absorption coefficient of the Russian crystal.
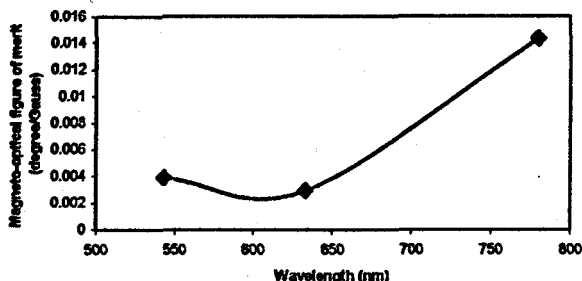
Figure 33. Figure of merit of the Russian crystal.

10. Task 8: Model hybrid package layout for design analysis.

Modeling was accomplished using FEMLAB to determine the magnetic field distribution in a commercial half bridge power module from Semikron (with a part number SK 100 MB10). This work was required because it was important to determine where to put the sensing tip in a power module. Figure 34 shows the mashes of finite element modeling of the Semikron module. Figure 35 shows the corresponding result of magnetic field distribution along the perpendicular (z) direction when one switch of the half bridge is ON and the other is OFF.
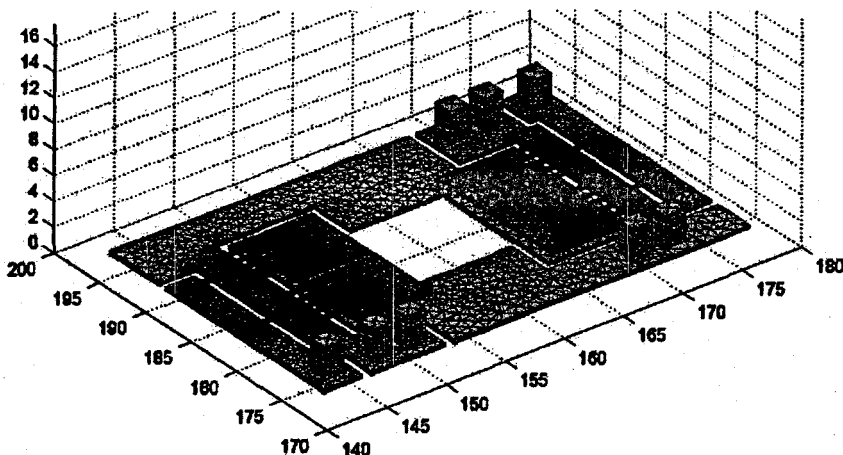
Figure 34. Finite elemental modeling of a Semikron power model.
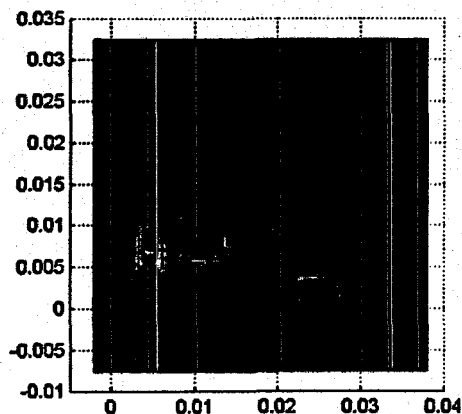
Figure 35. Modeling results--magnetic field distribution (z direction) in the Semikron power module when one switch is on.

20 V

1.2 Ω

S1

10 V

Sensing
crystal

S2

11. Task 9: Design the hybrid package sensor and optical support system.

Based upon the results of Task 8, it was possible to locate the optimum location for the magneto-optical sensor crystal. The figure to the left shows the actual Semikon module with the electro-optic element and a schematic of where it was located.
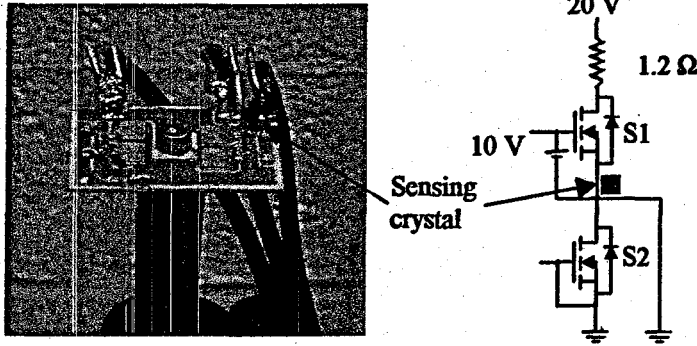
Figure 36. Sensor location and corresponding electrical schematic.

12. Task 10: Integrate and demonstrate the electro-optic hybrid power electronic module.

12.1 DC CURRENT SENSING

In our DC current experiment using the Semikron module, S1 was gated ON and S2 was kept OFF continuously as shown in Figure 36. Correspondingly, the magnetic field distribution is about the same as the modeling result in Figure 35. In the sensing test, the maximum current flowing through S1 is about 16 A when the voltage of power supply is 20 V. A LPE grown garnet crystal $(BiYbTb)_3Fe_5O_{12}$ (the American crystal) with a thickness of 0.475 mm was used at a wavelength of 780 nm. For comparison, the magnetic field in the power module was also measured directly by a Gauss/Tesla meter. The whole setup for DC current sensing is shown in Error! Reference source not found.. The maximum read from the Gauss/Tesla meter is about 15 G. In the test, the American crystal is put in at the point where the measured value reaches its maximum, which is coincident with the modeling result. In the experiment, the linear sensing signal changes are read from the dual-channel optometer. Using the Verdet constant about $5.33°/(G*cm)$ from the American crystal at 780 nm, which is determined in the characterization experiment, the calculated magnetic field-current curve is plotted in Figure 38. From Figure 38 one can see that the sensing data match well with the data read directly from the Gauss/Tesla meter.
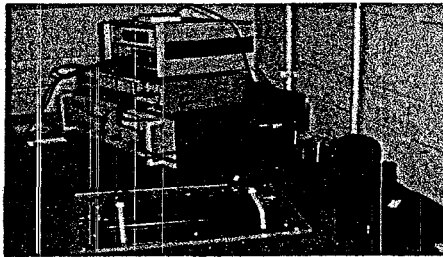
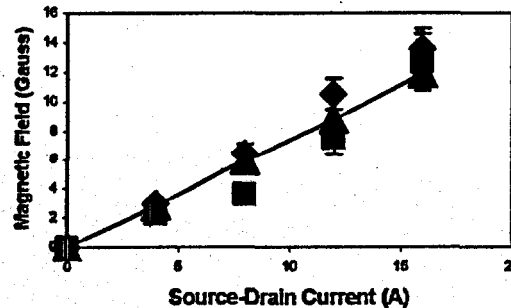*Figure 37. Setup for DC current sensing from the Semikron module.*

Figure 38. The DC current sensing data from the Semikron module. The square data are calculation results based on the dual-channel optometer readings, while the triangle data are read directly from a Hall-effect Gauss/Tesla meter with a resolution about 0.1 G.

12.2 AC CURRENT SENSING

In the AC current sensing experiment, an optical bench setup as shown in Figure 39 was used to test the AC responses of the sensing material. The Russian crystal and the 633 nm laser diode were used in this experiment. The diagrams of electrical circuit part and the optical sensing part of the setup are shown in Figure 40 and Figure 41, respectively. The controlling gate signals are from a simple gate driver circuit and is not included in Figure 40. The duty cycles are about 50% for each of the MOSFET switch and the testing frequency is from about 1 KHz to 10 KHz. Two current sensing signals are read from the voltage changes across the two 100 KΩ resistors connected to the x- and y-detectors as shown in Figure 41, respectively. The two sensing signals (Ch 1 and 2) were sent to a portable oscilloscope; the results for different frequencies are shown in Figure 42, Figure 43, and Figure 44. At the same time, the voltages read across the 1.2 Ω resistor (Ch 3) as shown in Figure 40 is also sent to the oscilloscope for comparison. Theoretically, when the polarizing directions of the polarizer and the beamsplitter have a cross orientation of 45 degree, the two sensing signals from the two photodiode-detectors should have identical shapes but have opposite AC magnitudes. Additionally, the shape should be also similar to the signals read from the 1.2 Ω resistor despite the difference in magnitudes. These situations are about correct at low frequencies under 10 KHz as shown in the oscillographs. However, at any frequency higher than 20 KHz, no sensing signals are detectable because of the following three reasons: 1) the signal of switching current itself attenuated much at higher frequency (see the changes of Ch 3 signals when frequency getting higher). 2) The switching current overshoots in the power module become higher at a higher frequency (also see Ch 3 signals). 3) The current detector electrical loops pick up the EMI noises from the switching electrical circuit and the situation become worse at a higher frequency (see Ch 1 and 2 signals).

Figure 39. Setup for getting signal changes from a commercial power module working at a continuous switching mode.
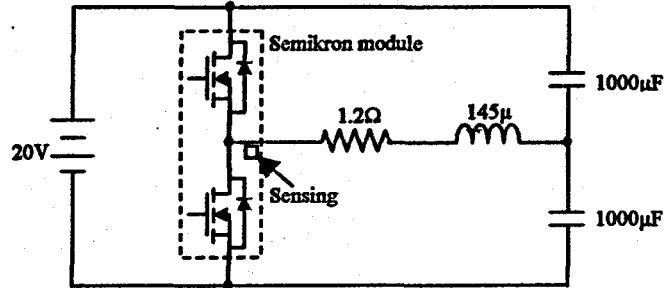

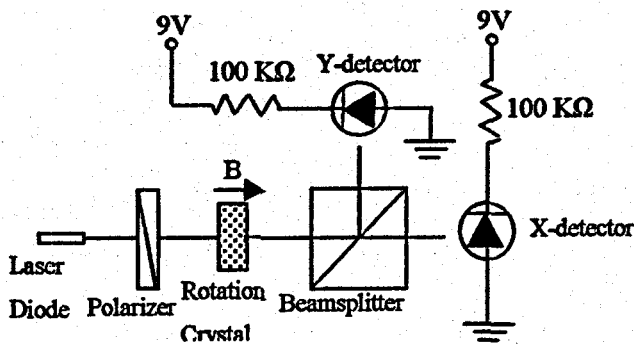Figure 40. The electrical circuit part of the AC current sensing test.

Figure 41. The optical sensing part of the AC current sensing test.
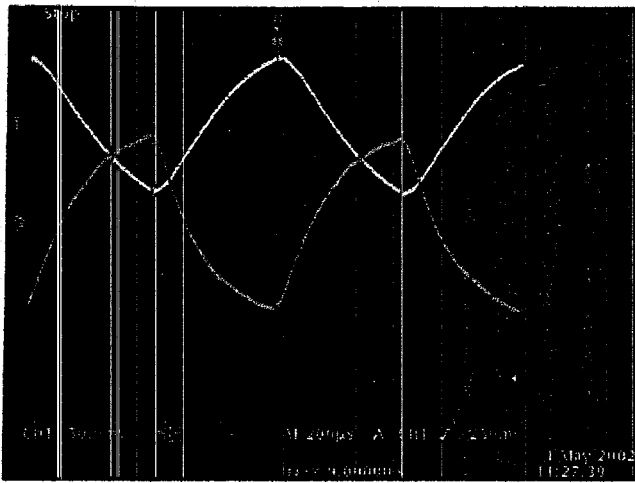
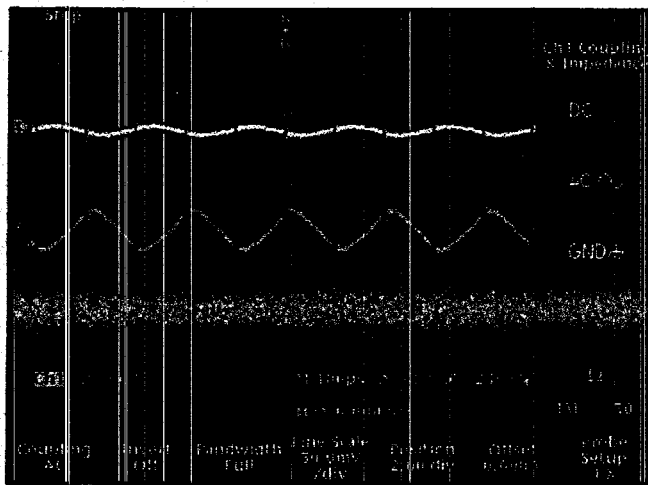*Figure 42. AC current sensing results from a portable oscilloscope at 1 KHz.*

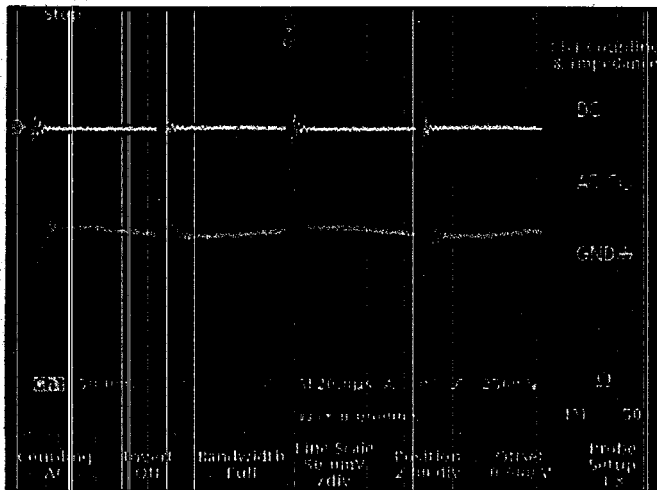*Figure 43. AC current sensing results from a portable oscilloscope at 5 KHz.*

Figure 44. AC current sensing results from a portable oscilloscope at 10 KHz.

12.3 CONCLUSION

The techniques for applications of magneto-optical current sensors in integrated power electronics modules (IPEMs) are investigated in this research report. Growth of garnet film by a sol-gel processing shows the possibility and viability to fabricate magneto-optical sensing probes directly in power devices. An optical bench for Faraday rotation characterization has been set up to determine the Verdet constants and figures of merits of sensing materials. The setup was successfully applied to two different types of Faraday crystals. Using the characterized crystals, a DC current sensing setup has been used to detect the magnetic field in a commercial power module. The results of the DC current sensing experiment from the power module match well with both finite element modeling and directly measuring results. Using the same commercial power module, techniques for AC current sensing were also investigated. The AC current sensing results show that the signals are detectable up to 10 KHz from the preliminary optical bench setup. The problems at higher frequencies that resulted are discussed and more experimentation in high-frequency applications is required. In summary, the preliminary investigations on magneto-optical sensing have shown that the sensors based on this technique could be very promising and effective for integration in the modern and advanced generation of IPEMs though much work still left to do.